On the origin of vesuvianite-rich rodingites from the Western Carpathians, Slovakia

Juraj Butek, Michel Grégoire, Ján Spišiak, Stéphanie Duchene, Richard Kopáčik

On the origin of vesuvianite-rich rodingites from the Western Carpathians, Slovakia

Juraj Butek [a,b,*], Michel Grégoire [b], Ján Spišiak [a], Stéphanie Duchene [b], Richard Kopáčik [a]

[a] Department of Geography and Geology, Faculty of Natural Sciences, Matej Bel University, Tajovského 40, 97 401 Banská Bystrica, Slovakia
[b] Géosciences Environnement Toulouse (GET), Université de Toulouse, UPS, CNRS, IRD, CNES, 14 Av. E. Belin, 31400 Toulouse, France

* corresponding author: juraj.butek@umb.sk; juraj.butek@get.omp.eu

Abstract

Rodingite represents a particular metasomatic rock type that occurs as dykes or lenses in association with serpentinized ultramafic rocks and typically consists of Ca-rich, often hydrated silicate minerals. Rodingites have been recognized as a source of information on fluid compositions and their circulation in both ocean floor and subduction environments. Yet, the nature of the protoliths, the chemistry and the origin of fluids, the details of fluid-rock interaction, and the metamorphic context remain often obscure. This work investigates some of these questions in the case of rodingites from the Western Carpathians through petrological, mineralogical and geochemical studies. Rodingites are here associated in the field with serpentinized tectonically dismembered bodies of ultramafic rocks embeded into Carboniferous metasediments. They mostly consist of vesuvianite, diopside, and hydrated garnet with minor titanite, chlorite, epidote, calcite and Fe-Ti oxides. Three successive hydrothermal events were recognized: 1) formation of diopside, vesuvianite and garnet, 2) formation of a second generation of vesuvianite and garnet together with titanite and minor chlorite, and 3) formation of a mineral assemblage consisting of epidote, chlorite and calcite. The first two events represent a pervasive and intense rodingitization process, whereas the third one represents late, channeled, fluid circulation under greenschist facies conditions. The presence of Fe-Ti oxides influences the mineralogy and the whole rock chemistry of the investigated rodingites. Rutile and ilmenite are commonly associated with titanite and garnet, and whole rock analyses can reach up to 9.2 wt.% TiO_2. Vesuvianite and garnet also incorporate a significant amount of titanium. The lack of primary minerals, the mineral composition as well as high CaO and low SiO_2 contents demonstrate high extent of Ca-metasomatism. The high modal amount of vesuvianite and the immobility of Al during metasomatic processes suggest that the protolith was relatively Al-rich. Taking into account the REE patterns of whole-rock and minerals, the high TiO_2 content and the local Fe-Ti-rich accumulations, we suggest that the protoliths were more or less Fe-Ti-rich gabbroic rocks initially occurring in association with the serpentinized ultramafic body.

Keywords: rodingitization, metasomatism, vesuvianite, gabbroic protolith, serpentinite, Western Carpathians

1 Introduction

Rodingites are generally very heterogeneous, light-coloured dense rocks consisting of Ca-rich often hydrated silicate minerals such as hydrated garnet, diopside, vesuvianite, epidote-zoisite, chlorite, or prehnite (Coleman, 1967; Li et al., 2004; Schandl et al., 1989), parageneses quite similar to typical Ca-skarns. Minor or accessory minerals are commonly represented by amphibole, titanite, calcite, rutile, and ilmenite. It is worth emphasizing that there is no exact definition of the term rodingite based on chemical, mineral, or textural characteristics because these tend to be highly variable. Consequently, a large variety of metasomatic and metamorphic rocks are called 'rodingites' in the literature (Coleman, 1967). The high content of Ca, low Si, and the similar process of formation are likely to be the only common attributes of rodingites.

Rodingite formation is a metasomatic process involving Ca enrichment and Si, Na and K leaching from a protolith (e.g. Koutsovitis et al., 2013; Laborda-López et al., 2020; Li et al., 2017, 2007; Tang et al., 2018). The protoliths of rodingites are most commonly mafic rocks (e.g. Koutsovitis, 2017; Li et al., 2017, 2004) or more rarely, other rock types including sedimentary or felsic lithology (Coleman, 1967; El-Shazly and Al-Belushi, 2004; Esteban et al., 2003; Normand and Williams-Jones, 2007). Most importantly, rodingites are in the field always associated with serpentinites (be it in ophiolitic sequences, in isolated tectonic fragments, or even at present-day ocean floor), and it is thus evident that the rodingitization process is linked spatially and temporally to serpentinization of ultramafic rocks (Bilgrami and Howie, 1960; Honnorez and Kirst, 1975). Rodingites occur as dykes, lenses or boudins within serpentinized ultramafic bodies (Li et al., 2017; Nishiyama et al., 2017; Schandl et al., 1989) and can also sporadically form at the contact between serpentinite and its surrounding sedimentary or metamorphic lithology (Coleman, 1967; El-Shazly and Al-Belushi, 2004).

Serpentinites are typically homogeneous and relatively sterile in their mineralogy and geochemical signature. Recent studies focusing on rodingite mineralogy and geochemistry show that rodingites can additionally provide useful information about the oceanic hydrothermalism. They allow to discuss the tectono-metamorphic evolution of the serpentinite (Laborda-López et al., 2018; Li et al., 2008), to define pressure-temperature conditions (Koutsovitis et al., 2013; Li et al., 2007, 2004; Zanoni et al., 2016), to determine geodynamic settings (Ferrando et al., 2010; Hu and Santosh, 2018; Wang et al., 2019), or even to resolve the age of the serpentinization process itself (Dubińska et al., 2004; Haws et al., 2021; Li et al., 2014). Furthermore, rodingites represent an effective indicator of the composition of fluids that circulate on the ocean floor and subduction zone environments (Duan et al., 2022; Salvioli-Mariani et al., 2020; Wang et al., 2019).

The most detailed studies of rodingites in the world are devoted to occurrences from Xigaze ophiolite in South Tibet (Dai et al., 2016; Duan et al., 2022, 2021; Li et al., 2017), from Zermatt-Saas ophiolites in the Alps (Li et al., 2008, 2004; Zanoni et al., 2016), and from ophiolites in Greece (Karkalis et al., 2022; Koutsovitis, 2017; Koutsovitis et al., 2013; Rogkala et al., 2022). In the Carpathian Mountains, several rodingitized rock occurrences were described by Hovorka et al. (1985) but until now only the occurrence in Dobšiná quarry has been examined in greater detail (Butek et al., 2021; Li et al., 2014; Putiš et al., 2016). Aluminium rich metasomatized samples were previously reported by Spišiak et al. (2018) from the Breznička-Bôrček serpentinite body located at ca. 70 km south-west from the Dobšiná occurrence. This work represents the first detailed petrographic, mineralogical, and geochemical investigation of

rodingites from this locality. It aims to shed light on the nature of the protoliths and the mineralogical imprints of the metasomatic processes.

2 Geological settings

The Carpathian Mountains represent a 1500 km long part of the Alpine orogenic belt located in central and eastern Europe. It has been formed by a series of Jurassic to Tertiary subduction and collision events, and its geology can be characterized by a complex structure with numerous thrust faults and nappes (Froitzheim et al., 2008). The Western Carpathians (WC), situated mainly in Slovakia, are longitudinally divided into three main tectonic zones: External, Central, and Internal Western Carpathians (Plašienka, 2018).

The External WC cover the territories of northern Slovakia, southern Poland, and eastern Czech Republic and comprise a Tertiary accretionary complex formed almost exclusively of thrusted sedimentary units. The boundary between the External WC and the Central WC is determined by the Pieniny Klippen Belt (Fig. 1a), a tectonic unit consisting of Jurassic to Early Cretaceous carbonate rocks towering from erosion of less resistant Upper Cretaceous and Paleogene marlstones and clay sediments. This zone represents a mark of the Late Cretaceous to Early Tertiary south-oriented closure of the Penninic (Magura) ocean domain and is thus considered as the main fossil plate boundary of the WC, despite the lack of evidence for ophiolite rocks. The Central WC form the core of the Carpathian orogeny and are longitudinally subdivided on the basis of north-vergent thick-skinned thrust sheets into the Core mountains Belt, the Vepor Belt and the Gemer Belt (Fig. 1a). The first two consist dominantly of Paleozoic crystalline basement rocks (granitoids and gneisses of Variscan origin) covered by Late Paleozoic and mainly Mesozoic sedimentary sequences. The Gemer Belt represents the structurally highest tectonic zone of the WC. It consists mainly of low-grade metamorphic rocks of the Paleozoic age (Gemeric superunit) that are overlain by several Mesozoic thin-skinned nappe units belonging to the Internal WC. The lowermost of these, the Meliata unit, consists of deep-water sediments and distinct blueschist facies rocks, and represents evidence of the Meliata (Meliata–Hallstatt) ocean domain which closed during the Middle to Upper Jurassic period (Kozur, 1991; Plašienka, 2018; Plašienka et al., 2019). Dismembered ophiolitic mélanges include numerous serpentinized ultramafic bodies that are commonly associated with carbonate sediments of Triassic age and are nowadays irregularly dispersed over the Gemeric superunit (Fig. 1a). However, there are also some serpentinite occurrences tectonically associated with pre-Mesozoic (Carboniferous) metasediments and it remains hard to definitely resolve their provenance (Hovorka et al., 1985, 1983). Locally, rodingitized rocks were reported from these serpentinized bodies, but for now they were only partially investigated (Butek et al., 2021; Hovorka et al., 1985; Li et al., 2014). One of these occurrences is represented by the outcrop at Breznička–Bôrček.

The Breznička–Bôrček hill (sometimes referred to as Bôrček or Kalinovo) is located between the two villages of Breznička and Kalinovo at GPS coordinates 48°24'16.8"N, 19°43'45.9"E (Fig. 1b). The area was rigorously studied in the late 1970s with the objective of evaluating the occurrence of chrysotile asbestos and its potential exploitation. At the end, the asbestos from Bôrček has never been industrially mined, but numerous boreholes and exploration galleries allow to precisely map the serpentinized ultramafic bodies (Fig. 1c,d; Zlocha et al., 1980). However, the region is dominated by Cenozoic sedimentary cover (Fig. 1b) and consequently the interpretation of geological settings on a larger scale remains intricate. The only emerging

unit of the Gemericum is a Carboniferous metasedimentary complex (Turnaisian-Visean, based on palynological study; Bajaník and Planderová, 1985). These metasediments have a thickness of 450 to 1300 m and are tectonically northward thrusted on Permian/Early Triassic Veporic sedimentary cover sequences.

Carboniferous metasediments are dominated by variegated phyllite rocks affected by low-grade greenschist facies metamorphism (Sassi and Vozárová, 1987) and represent the lithology surrounding the serpentinite bodies (Fig. 1c, d). The most common metasedimentary rock is represented by biotite-chlorite phyllite, additionally consisting of quartz, albite, carbonates, titanite and other minor minerals. Locally occurring graphite-rich sequences (not shown on the map), which crop out mainly at the base of serpentinite bodies, further demonstrate their variegated character. Iron sulfides with presumably syngenetic origin were also described in significant quantities (Zlocha et al., 1980). It is worth noting the presence of hydrothermally altered mafic rocks that occur locally at the base of serpentinite bodies (Fig. 1c, d). This mafic rock is intensively altered mostly at contact with serpentinite by the processes of steatitization and carbonatization and consists of turquoise amphibole, epidote group minerals, biotite, titanite, albite, chlorite, quartz, and calcite. The rock is particularly characterized by a high modal amount of titanite (up to 8 %) and epidote group minerals (up to 10 %). Despite the lack of preserved primary minerals, Zlocha et al. (1980) proposed that the original rock was probably a (porphyric) diabase.

Serpentinite bodies occurring at Bôrček in a SW-NE oriented zone have a full-length of 2250 m (Fig. 1c). Serpentinites are exposed as numerous tectonic slices folded into the metasedimentary sequence. They are often dismembered and displaced by tectonic faults. The thickness of these serpentinite bodies varies from a few to a hundred meters; their dip is also variable but generally oriented to the SE (Fig. 1d).

The serpentinites are intensively steatitized mainly at the contact with the surrounding metasedimentary rocks. Smaller serpentinite bodies are almost completely transformed into talc-rich rocks. In addition to this alteration, serpentinite rock is often affected by chloritization, amphibolitization, and, to a lesser extent, carbonatization. These processes are typical not only for the outer parts of the serpentinite bodies, but also affect the fault zones within them. Intense serpentinization transformed the original peridotite rock to the extent that no primary ultramafic minerals (olivine and pyroxene) were preserved, and even pseudomorphs are very scarce. The rock matrix is typically made up of small unoriented aggregates of serpentine group mineral (mainly antigorite). Considering oxide minerals, magnetite is very abundant and may constitute up to 10-15 % of a rock sample (Zlocha et al., 1980).

Rodingite-like rocks were originally reported from one borehole (BV-26, Fig. 1c) at the lower contact between serpentinite and biotite-chlorite phyllite but also as a xenolith enclosed in the serpentinite (Zlocha et al., 1980). They show an aphanitic texture, heterogeneous light greenish-brownish color, and consist of ‘Ca-garnet, pyroxene, vesuvianite, prehnite, minerals of the epidote group and others’ (Hovorka et al., 1983). Unfortunately, these rodingites were not studied in more detail and were not archived. The samples analyzed in the present work were collected from the dumps where they are associated with serpentinites, both materials extracted from exploratory galleries and today accumulated on the north-western slope of the Bôrček hill (Fig. 1c).

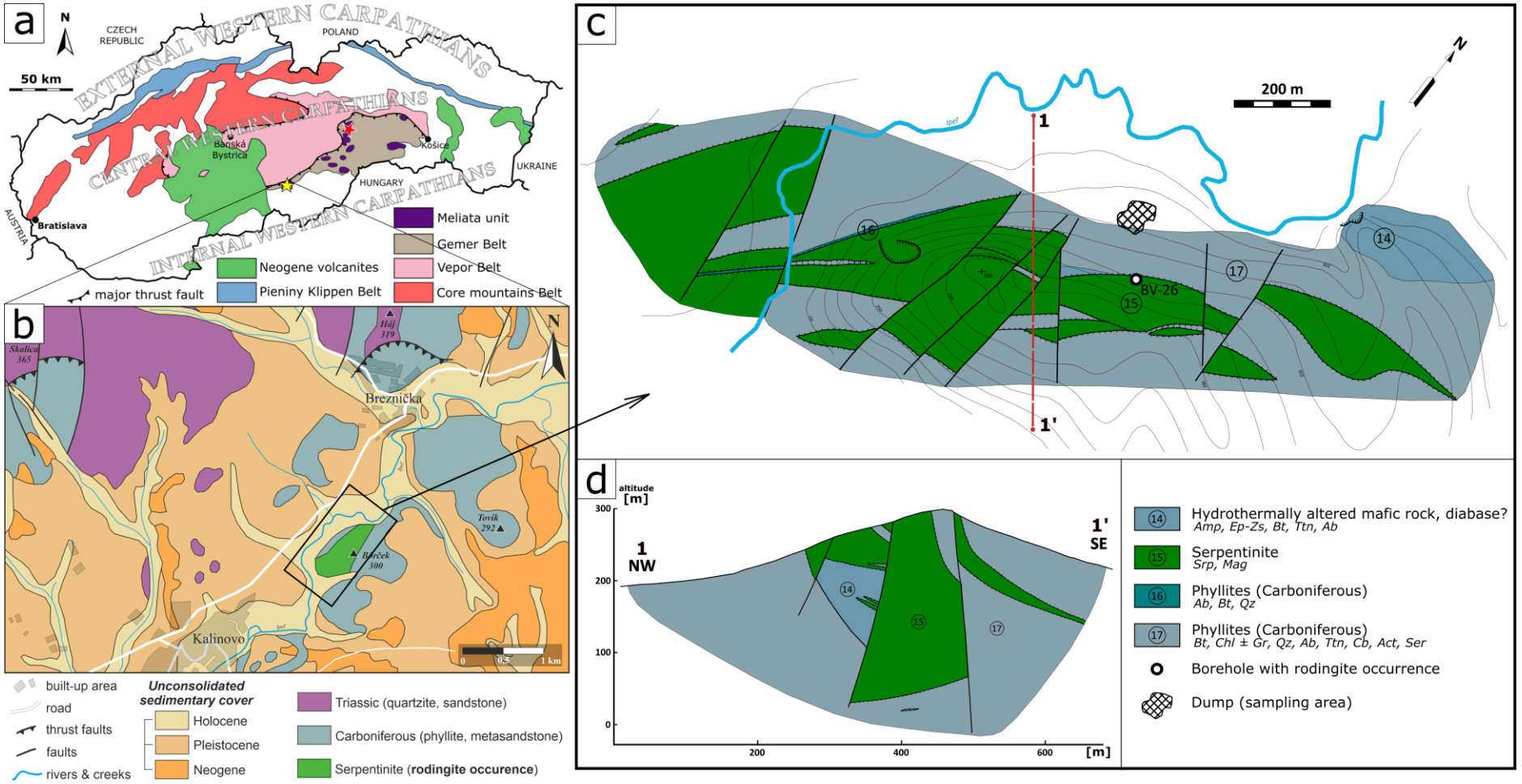

Figure 1 a) Geological sketch map of the Central Western Carpathians in Slovakia. The yellow star indicates the investigated locality. The red star indicates rodingite occurrence in Dobšiná already described in the literature (Li et al. 2014; Putiš et al. 2016; Butek et al. 2021). b) Simplified geological map of the Breznička-Kalinovo region (modified after "Geologická mapa Slovenska [online], ŠGÚDŠ," 2013). The serpentinized ultramafic rocks are associated with a carboniferous metasedimentary complex, and a substantial part of the region is covered by unconsolidated Cenozoic sediments. c) Detailed geological map of the Breznička-Bôrček area without sedimentary cover (modified after Zlocha et al., 1980). d) Geological cross-section 1–1' in the most complex zone. Serpentinite occurs in the form of numerous tectonically dismembered bodies folded into the metasedimentary sequence consisting of variegated phyllites. Rodingitized rocks were originally reported from the drill core of the BV-26 well; however, the investigated samples come from a nearby dump area.

3 Analytical Methods

Wavelength-dispersive spectroscopy (WDS) microprobe analyses including composition maps of rodingite minerals were performed on thin sections using a Cameca SXFive operated at the Centre de microcaractérisation Raimond Castaing, CNRS, Toulouse, France. A part of the electron microprobe analyses was acquired at the Earth Science Institute of the Slovak Academy of Science, Banská Bystrica, Slovakia, using a JEOL JXA-8530FE instrument. An accelerating voltage 15 kV, current 20 nA, and spot size 2-5 μm were used at both institutions. The processing of the microprobe analyses of garnet and the recalculation of the mineral formula were complicated by the presence of OH in the crystal structure and presumably both iron oxidation states (Fe^{2+} and Fe^{3+}). Hydration was confirmed by microRaman measurements (Fig. S1). The H_2O content in the garnets was calculated from the Si deficiency at the tetrahedral site ($Si^{4+} + H^{+}/4 = 3$) after normalization to 8 cations (including H^{+}), considering all iron to be Fe^{3+}. Recalculation of the vesuvianite formula was based on 50 cations and 78 anions (156 charges), considering all iron to be Fe^{3+}. The recalculation of chlorite analyzes was performed using the WinCcac software from Yavuz et al. (2015). Other mineral formulas were recalculated using traditional normalization schemes. Graphical representations of the microprobe results were made using Golden Software Grapher.

Trace element content in rodingite minerals was measured using an ELEMENT XR High Resolution ICP-MS (Thermo Scientific) coupled with a New Wave Research NWR213 Nd YAG 213 nm laser ablation unit operated at the Géosciences Environnement Toulouse laboratory, Observatoire Midi Pyrénées, Toulouse, France. The counting time for one analysis was 120 s (30 s on gas blank to establish background, then 60 s for data acquisition followed by 30 s washout). The laser was set for energy 4-5 J/cm^2, 5-10 Hz repetition (pulse) rate, and 20-30 μm spot size. The reference materials NIST SRM 610 and NIST SRM 612 were used as external standards to control accuracy. Rounded values determined by electron microcrobe analyses of a major oxide served as an internal standard for each mineral phase: vesuvianite (36 % CaO), garnet (34,5 wt% CaO), diopside (26 wt% CaO), calcite (58 % CaO), chlorite (32 % MgO). The relative precision and accuracy for a laser analysis range from 1 to 10 % for most of the elements, but for Nb and Ta they are close to 15%. The theoretical detection limits for each element are in the range of 10–60 ppb except for Sc and V (100 ppb), Ti (2 ppm) and Ni and Cr (0.7 ppm). Data reduction and processing was performed using Glitter software (Griffin et al., 2008).

About 50 g of each sample were crushed manually and then pulverized in dry agate ball grinding jars in a Mill PM200 (RETSCH) for 4 hours. Whole-rock analyses of 7 rodingites powdered samples were performed in 2019 using several analytical methods (package LF200) at Acme Laboratories Ltd., Vancouver, Canada. The major oxide compositions were measured using lithium borate fusion coupled with ICP-AES analysis with a detection limit 0.01 % for all oxides except Cr_2O_3 (0.002 %) and Fe_2O_3 (0.04 %). The compositions of trace elements were evaluated using ICP-MS analysis with a detection limit ranging from 0.01 to 1 ppm depending on the element, with an exception for V (8 ppm). Total C and S contents were determined using LECO combustion analysis with a detection limit of 0.02 %. The accuracy was externally verified with an analysis of a reference diorite sample (DR-N; Govindaraju and Roelandts, 1989). The difference between standardized and measured values do not exceed 5 % for major oxides and 15 % for trace elements (Table S1). The ratio of iron oxidation states was determined

by analytical chemistry at the Department of Chemistry, Matej Bel University, Slovakia, using the procedure developed by Roth et al. (1969).

4 Results

4.1 Petrography

Rodingite samples from Bôrček are dense, medium-grained rocks with irregular patches of green, grey, cream, and even dark color (Fig. 2a). This heterogeneous coloring is related to the distribution of the main minerals with vesuvianite and clinopyroxene forming centimeter scale aggregates and chlorites in veins of different sizes. In details, rodingites consist of vesuvianite, clinopyroxene, garnet, titanite, epidote, chlorite, calcite, and Fe-Ti oxides. The heterogeneity between samples can be illustrated by the approximative modal compositions (Tab. 1). The modal proportions of vesuvianite, for example, may vary from accessory to dominant reaching up to 80 %. Particularly, based on the presence of Fe-Ti oxides, namely rutile and ilmenite, the studied samples are classified into two groups: 1) 'Ti-rich' samples with observed Fe-Ti oxides (FBR-55, FBR-56, FBR-57 and FBR-64) and 2) 'Ti-poor' samples without Fe-Ti oxides (FBR-61, FBR-63 and FBR-70).

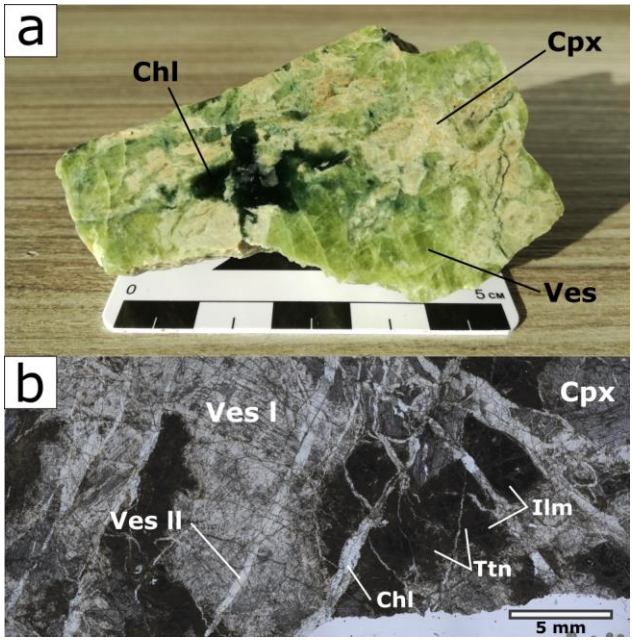

Figure 2 a) Coarse-grained rodingite (sample FBR-63) consisting of vesuvianite (green), diopside (cream-colored), and clinochlore (greenish black). B) Rodingite thin section (sample FBR-57) illustrating hydrothermal textures (normal light). Mineral abbreviations are after (Whitney and Evans 2010).

*Table 1 Rough modal composition of analyzed samples: *** major (> 30 %), ** minor (> 5 %), * accessory (< 5 %). Mineral abreviations are after Whitney and Evans (2010).*

Sample	Ves	Cpx	Grt	Ttn	Ep	Chl	Cal	Rt,Ilm
FBR-55	***	*	**	*	***	*	*	*
FBR-56	*	*	***	**	**	*	*	**
FBR-57	***	***	*	**	*	*		*
FBR-61	***	*	*	*		*	*	
FBR-63	***	***	*	*		*		
FBR-64	***	**	*	**		*	*	*
FBR-70	**	*	*	*	***	***	*	

All rock samples display characteristic textures of intense hydrothermal alteration with numerous replacement reaction features and disordered fractures and veinlets (Fig. 2b). The size of these veinlets is typically several hundreds of μm but can occasionally reaches 2 mm. The veinlets are most commonly filled with coarse vesuvianite, but chlorite filling is also frequent. Carbonate veinlets occur in some spots. It is worth to note that the complex cross-cutting relationships of these structures often obscure their relative chronology. Nevertheless, it was possible to distinguish two generations for most mineral species. These successive generations will be numbered I and II. Note that this does not refer to successive paragenesis.

Vesuvianite represents the most abundant mineral (40 – 80 %) except in two samples (Tab. 1). Macroscopically, it displays an intense green color (Fig. 2a), but in thin sections it appears colorless. At least two generations of this mineral were recognized based on textural observations. Vesuvianite I commonly displays a microcrystalline texture and typically occurs in association with clinopyroxene (Fig. 3a, b) and lesser garnet (Fig. 3c; 4a, b). Minor amounts were also observed enclosed within the epidote. Sometimes, it displays a very particular fibrous radial texture (Fig. 3d). Vesuvianite II occurs exclusively in Ti-rich samples and occurs in veins that crosscut mainly vesuvianite I rich domains. It displays a distinct coarser texture than vesuvianite I (Fig. 2b, 3e). Vesuvianite II can be the only mineral that fills those veins, but it frequently occurs in association with chlorite (Fig. 4c).

Clinopyroxene occurs as significantly altered, centimeter large colorless crystals in typical association with vesuvianite I (Fig. 3a, b). Clinopyroxene grains are commonly rimmed with garnet (Fig. 3f, g; 4d). Rare tiny crystals were also identified within the epidote. The texture of large clinopyroxene grains regularly features characteristic cleavage lamellae where the interstices are generally filled with chlorite associated with inclusions of garnet and vesuvianite (Fig. 4e). Crystals often present internal deformation marked by ondulatory extinction (Fig. 3b), misorientation and recrystallization of small grains at crystal boundaries (Fig. 3e).

Garnet occurs in multiple distinguishable forms. In thin section, it always displays an orangish colour contrasting with other major colorless mineral phases. We refer to garnet I and garnet II as two main generations of garnet occurrence. Garnet I evidences a particular kind of 'poikilitic' texture where small isometric but rather anhedral crystals are dispersed within the vesuvianite I matrix (Fig. 3c, 4a). Similarly to vesuvianite and clinopyroxene, minor amounts of this type of garnet are enclosed in the epidote. Garnet II represents the most widespread type. Its development is typically pervasive, but rare vein-like structures are also observed. It seemingly

forms a rim around opaque minerals in close association with titanite (Fig. 3h; 4f, g), and less frequently forms a rim around or crosscuts clinopyroxene (Fig. 3f, g; 4d, h). Furthermore, subhedral forms of garnet occur sporadically in association with titanite in late calcite veins (Fig. 3i).

Titanite is common, but its occurrence is noticeably restricted to areas with oxide minerals (namely rutile and ilmenite, Fig. 4g, i). It occurs as 100-200 μm thick rims or as filling of cracks occurring within those minerals, in intimate association with garnet II. While it is evident that the association titanite + garnet forms reaction rims around oxide minerals, titanite commonly occurs in contact with oxides while garnet forms the outer part of those rims (Fig. 3h; 4f, g). Rarely, euhedral crystals of titanite occur in association with garnet in late calcite veins (Fig. 3i).

Rutile and ilmenite represent the Fe-Ti oxides and are present only in the Ti-rich samples (Tab. 1). They form anhedral and commonly fractured aggregates of sub-micrometric intergrowths (Fig. 4g) irregularly dispersed within the samples. In the oxide aggregates, rutile and ilmenite appear as isolated anhedral crystals but also sometimes in composite grains consisting of a rutile core surrounded by an ilmenite rim (Fig. 4i).

Scarce tiny grains of apatite and Zr-bearing minerals (zircon, baddeleyite, zirconolite) but rarely also sulfides such as pyrite, chalcopyrite, millerite, and polydymite were identified. The occurrence of all these accessory phases together with scarce perovskite is closely associated with the Fe-Ti oxides.

Epidote forms large euhedral crystals (up to 2 mm, (Fig. 3j) with light pinkish or yellowish coloring and pronounced pleochroism. Its modal distribution varies significantly from one sample to another. It occurs in a well-equilibrated association with chlorite and minor calcite (Fig. 4j). Large epidote crystals frequently enclose small irregular relics of vesuvianite, clinopyroxene and garnet (Fig. 3j, 4j).

Chlorite can be classified into three generations on the basis of its petrographic features and mineral associations. Sometimes it displays a light greenish colour, but most commonly chlorite crystals are colourless. Chlorite I occurs as vein filling in association with vesuvianite II and forms large crystal aggregates (up to 1 mm in size, Fig. 3g). Chlorite II occurs in association with epidote and calcite and generally exhibits a microcrystalline texture (Fig. 4j). Finally, chlorite III fills most of the fractures and interstices in the main minerals, presumably as the main result of their late alteration (Fig. 4e).

Three generations of calcite have been distinguished. Rare calcites I were identified in association with oxide minerals (Fig. 4g). Calcite II occurs in the above mentioned association with epidote and chlorite II (Fig. 4h, j). Finally, calcite III occurs in late carbonate vein filling, occasionally in association with subhedral garnet II and/or titanite (Fig. 3i).

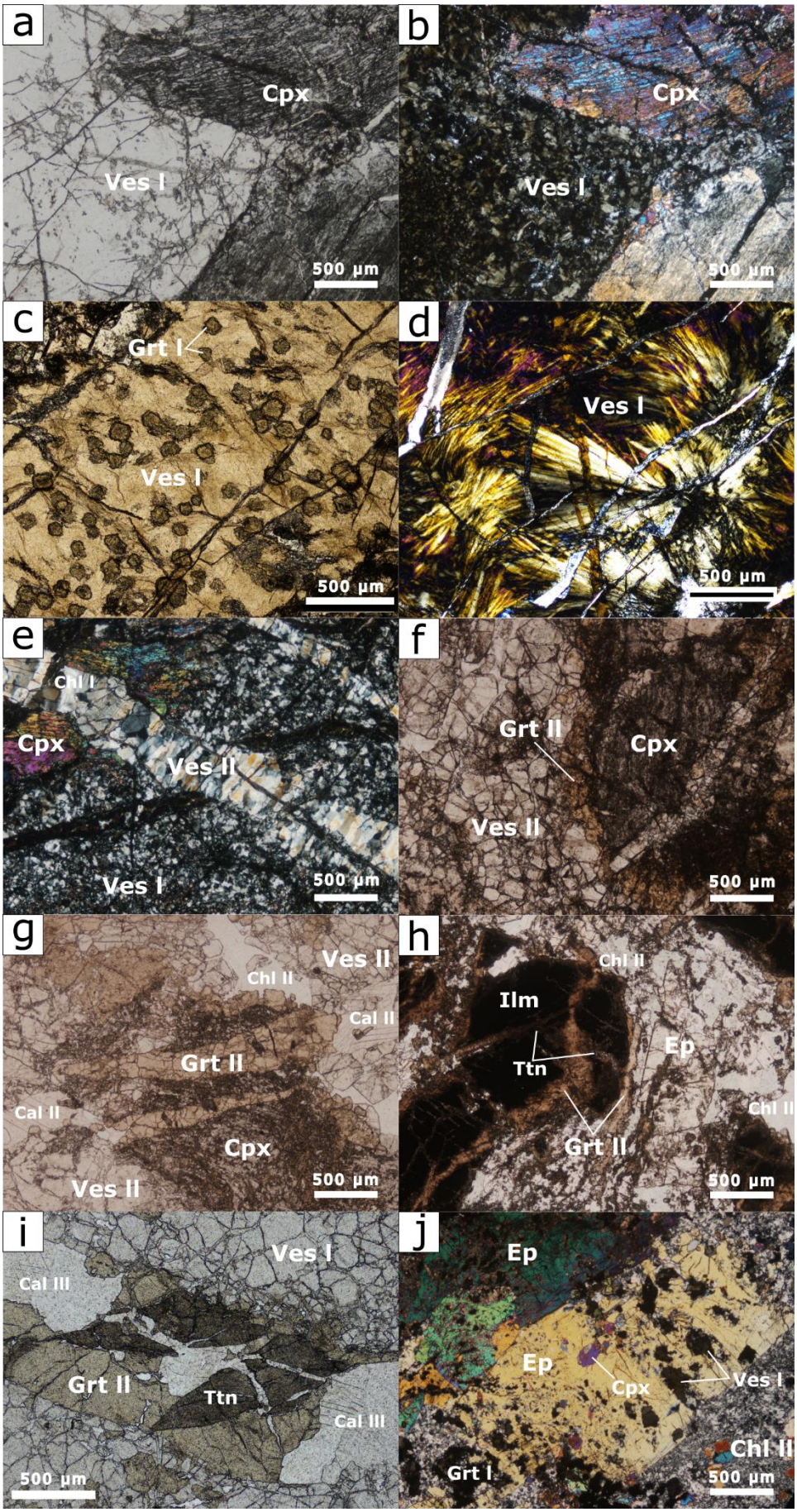

Figure 3 Photomicrographs of key rock textures and minerals (sample label in brackets). a, b) Predominant metasomatic assemblage consisting of vesuvianite I and clinopyroxene, PPL and XPL, respectively (FBR-63). c) Isometric garnet I grains in vesuvianite I matrix, PPL (FBR-55). d) Particular fibrous radial texture of vesuvianite I, XPL (FBR-63). e) Vesuvianite II vein crosscutting through primary vesuvianite I and clinopyroxene assemblage, XPL (FBR-57). f, g) Garnet II as rims and in fractures in clinopyroxene crystal, PPL (Borcok2). h) Oxide-rich spot crosscut and rimmed by titanite and garnet II, PPL (FBR-55). i) Subhedral forms of garnet II and titanite in a late calcite III vein, PPL (Borcok2). j) Main rodingite mineral relics (vesuvianite I, clinopyroxene, garnet I) enclosed within coarse-grained epidote, XPL (FBR-70). Mineral abbreviations are after (Whitney and Evans 2010).

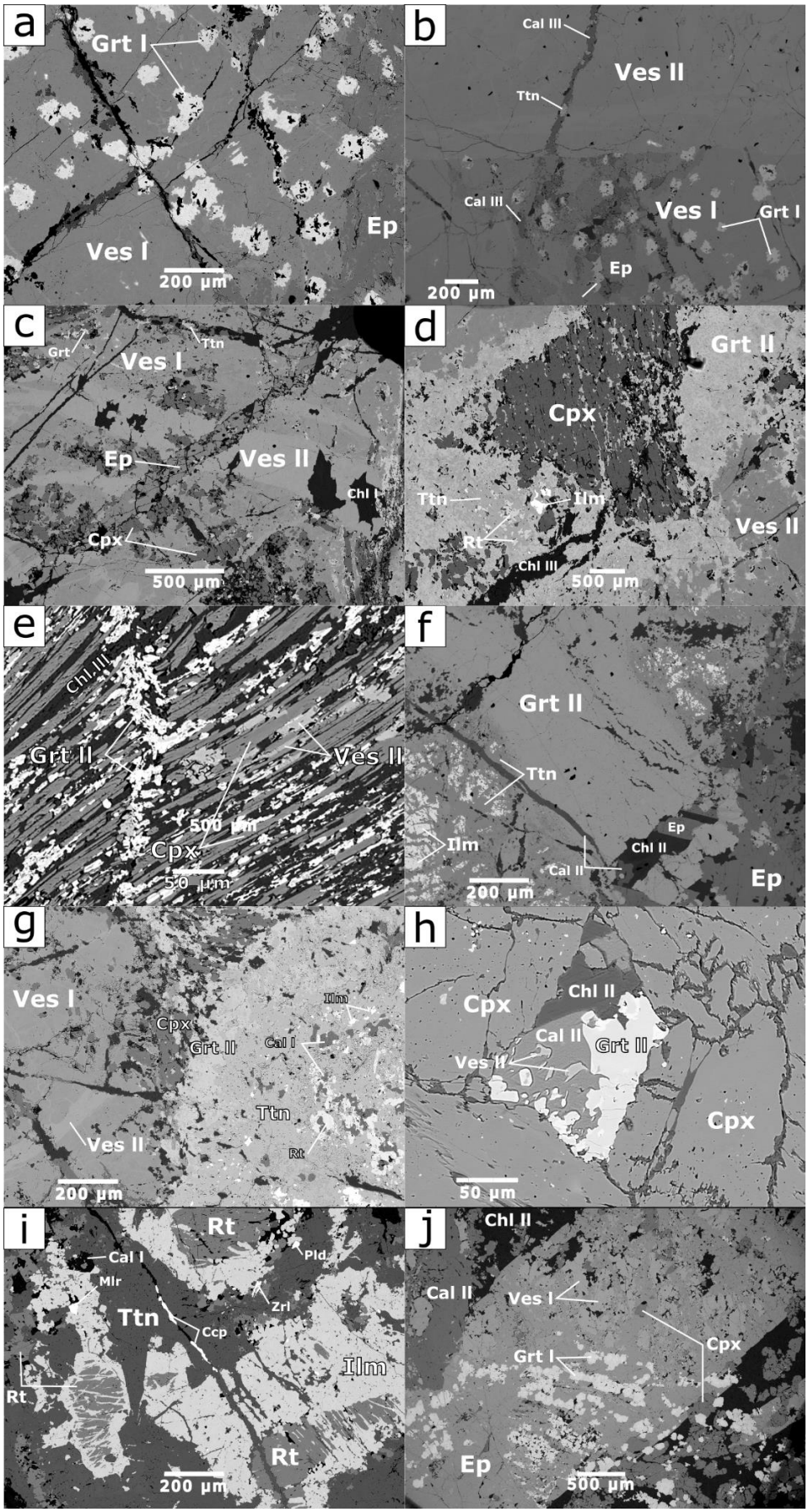

Figure 4 BSE images of key rock textures and minerals (sample label in brackets). a) Isometric garnet I grains in a matrix of vesuvianite I (FBR-55). b) Contrasting vesuvianite generations. Vesuvianite I contains isometric garnet grains while vesuvianite II does not contain other mineral phases (FBR-55). c) Epidote crystal crosscutting two generations of vesuvianite (FBR-57). d) Altered clinopyroxene crystal rimmed by garnet II, titanite, and relics of Fe-Ti oxides (FBR-57). e) Clinopyroxene lamellae crosscut by a garnet II vein. The interstices are dominantly filled with chlorite with minor garnet and vesuvianite (I-17B). f) Large garnet II associated with ilmenite relics and titanite. The bottom right corner is replaced with an epidote + chlorite ± calcite II assemblage (FBR-55). g) Titanite enclosing Fe-Ti oxide relics with calcite I. Garnet II forms a rim around this assemblage. Two vesuvianite generations are also distinguishable (Borcok2). h) Garnet II + vesuvianite II + chlorite II + calcite II association enclosed in clinopyroxene (BR-3). i) Fe-Ti oxide aggregate consisting of rutile partly replaced by illmenite in a titanite matrix (FBR-57). j) Main rodingite minerals (vesuvianite I, clinopyroxene, garnet I enclosed within a late epidote + chlorite II ± calcite II association (FBR-70). Mineral abbreviations are after (Whitney and Evans 2010).

4.2 Mineral chemistry

Vesuvianite is characterized by variable content in MgO (1.5 – 3.5 wt.%), Al_2O_3 (9.9 – 19.8 wt.%), total iron expressed as FeO (1.7 – 6.2 wt.%) and TiO_2 (0 – 7.3 wt.%) (Tab. 2, Tab. S2). Volatile species such as F and Cl are not present in detectable amounts. Vesuvianite I and vesuvianite II show a significant difference in chemical composition (Fig. 5). Vesuvianite II is lower in Al_2O_3 (< 15 wt.%) and generally higher in TiO_2 (> 1.5 wt.%), FeO_{total} (> 3.5 wt.%) and MgO (> 2.6 wt.%) than vesuvianite I. The two vesuvianite generations and their compositional variations are also easily identified in the binary discrimination diagram MgO vs Al_2O_3 (Fig. S3). Considering that all iron is Fe^{3+}, the simplified average structural formula of vesuvianite I and vesuvianite II can be expressed as $Ca_{19.05}(Al_{9.49}Mg_{1.61}Fe^{3+}_{1.46}Ti_{0.37}Mn^{2+}_{0.04}V_{0.01})_{\Sigma 12.98}(SiO_4)_{9.94}(Si_2O_7)_{4.00}O_{1.81}(OH)_{8.42}$ and as $Ca_{18.99}(Al_{6.90}Mg_{2.31}Fe^{3+}_{1.95}Ti_{1.78}Mn^{2+}_{0.03}V_{0.01})_{\Sigma 12.98}(SiO_4)_{10.02}(Si_2O_7)_{4.00}O_{2.36}(OH)_{7.56}$, respectively.

The content of rare earth elements (REE) evidences a distinct enrichment relative to the CI chondrite with a significant positive Eu anomaly in both vesuvianite types (Fig. 6a, c; Tab. 3). Vesuvianite I displays generally flat or slightly increasing REE pattern (La_n/Lu_n = 0.7 in average, *n* = 21). By contrast, most vesuvianite II REE patterns display a decreasing trend from LREE to HREE (La_n/Lu_n = 2.16 in average, *n* = 14). Vesuvianite I is slightly poorer in REE (Σ_{REE} = 2 – 29 ppm; 15 in average, *n* = 21) than vesuvianite II (Σ_{REE} = 2 – 110 ppm; 38 in average, *n* = 14). Trace element spider diagrams display depletion in Rb, Ba, and Th but enrichment in most trace elements within the range 1-10 times relative to CI chondrite (Fig. 6b, d). Sr and Ti commonly display positive anomalies. Interestingly, vesuvianite II spectra differ from vesuvianite I spectra by a larger variability, in particular, they display frequent U and Ti positive anomalies and extreme positive or negative anomalies in Nb, Ta, Zr, and Hf.

Clinopyroxene exhibits a relatively homogeneous composition characterized by high CaO and MgO content, resulting in the average structural formula $Ca_{1.01}Mg_{0.91}Fe^{2+}_{0.07}Si_{2.00}O_6$ ($Wo_{51}En_{46}Fs_{03}$). According to the Morimoto discrimination diagram (1988), these pyroxenes are classified as diopsides (Fig. 7). Diopside Mg# [Mg/(Mg+Fe)] varies within the 0.89-0.96 interval. Several electron microprobe profile analyses were performed in order to identify the compositional evolution, but no systematic core-to-rim zonations were observed. Diopside is very poor in trace elements. Most LA-ICPMS analyses display depletion relative to CI chondrite, and most element values are close to the detection limit.

264 *Table 2 Selected major oxides composition (wt.%) and structural formula of vesuvianites and garnets. Additional analyses are available in Table S1.*

	Ves I			Ves II			Grt I			Grt II		
Point	26 / 1.	2 .	43 / 1 .	53 / 1 .	44 .	2 .	46 / 1 .	68 / 1 .	83 / 1 .	10 .	60 .	29 / 1 .
Sample	FBR-57	FBR-63	FBR-70	FBR-57	ABorcok2	FBR-55	FBR-70	FBR-55	FBR-55	BR-3	ABorcok2	FBR-57
SiO_2	36.21	37.00	36.97	36.21	36.39	36.65	36.20	35.57	35.93	35.10	35.56	34.52
TiO_2	0.16	0.01	0.73	4.78	7.30	2.85	0.75	0.61	1.15	4.68	2.65	5.11
Al_2O_3	17.13	19.83	16.40	12.27	11.31	12.39	10.21	4.88	4.17	6.43	3.60	6.89
Cr_2O_3	b.d.l.	b.d.l.	0.00	0.01	0.02	b.d.l.	0.05	b.d.l.	0.04	0.20	0.03	0.03
V_2O_3	b.d.l.	b.d.l.	0.02	0.08	b.d.l.	0.03	0.02	b.d.l.	b.d.l.	b.d.l.	b.d.l.	b.d.l.
$FeO_{tot.}$*	3.45	1.70	4.06	4.30	3.60	5.75	15.35	21.16	21.54	16.86	22.76	14.32
MnO	0.02	0.10	0.08	0.08	0.11	0.09	0.61	b.d.l.	0.07	0.63	0.19	0.12
MgO	2.24	1.50	2.14	3.01	3.15	2.95	0.12	0.05	0.14	0.21	0.19	0.20
CaO	35.67	36.32	35.83	35.51	35.91	35.64	34.17	34.40	34.63	34.62	34.53	34.62
Na_2O	b.d.l.	b.d.l.	0.03	0.01	b.d.l.	0.01	0.06	0.01	0.02	b.d.l.	b.d.l.	0.02
K_2O	0.00	b.d.l.	b.d.l.	0.00	b.d.l.	b.d.l.	0.03	0.03	b.d.l.	b.d.l.	b.d.l.	b.d.l.
Total	94.87	96.48	96.26	96.26	97.79	96.38	97.59	96.70	97.69	98.72	99.51	95.83
H_2O**	2.60	2.49	2.47	2.24	2.03	2.41	0.95	0.58	0.49	1.72	1.25	1.42
recalculated structural formula												
Si^{4+}	17.93	17.95	18.13	18.01	17.92	18.16	2.87	2.92	2.93	2.77	2.83	2.81
$H^+/4$							0.13	0.08	0.07	0.23	0.17	0.19
Ti^{4+}	0.06	0.00	0.27	1.79	2.70	1.06	0.04	0.04	0.07	0.28	0.16	0.31
Al^{3+}	9.99	11.34	9.48	7.19	6.57	7.23	0.96	0.47	0.40	0.60	0.34	0.66
Cr^{3+}	-	-	0.00	0.00	0.01	-	0.00	-	0.00	0.01	0.00	0.00
V^{3+}	-	-	0.01	0.03	-	0.01	0.00	-	-	-	-	-
Fe^{3+}	1.43	0.69	1.67	1.79	1.48	2.38	1.02	1.45	1.47	1.11	1.52	0.97
Mn^{2+}	0.01	0.04	0.03	0.03	0.05	0.04	0.04	-	0.00	0.04	0.01	0.01
Mg^{2+}	1.65	1.09	1.56	2.23	2.31	2.18	0.01	0.01	0.02	0.02	0.02	0.02
Ca^{2+}	18.93	18.88	18.83	18.92	18.95	18.92	2.91	3.03	3.03	2.93	2.95	3.02
Na^+	-	-	0.02	0.01	-	0.01	0.01	0.00	0.00	-	-	0.00
K^+	0.00	-	-	0.00	-	-	0.00	0.00	-	-	-	-
Σ cations	50.00	50.00	50.00	50.00	50.00	50.00	8.00	8.00	8.00	8.00	8.00	8.00
O^{2-}	67.73	67.81	68.52	68.02	67.70	68.62	12.03	12.00	12.01	12.14	12.09	12.13
$(OH)^-$ *(W)*	8.59	8.05	8.07	7.41	6.68	7.97						
O^{2-} *(W)*	1.68	2.14	1.41	2.56	3.62	1.41						
Σ anions	78	78	78	78	78	78	12.029	11.998	12.006	12.140	12.087	12.129

b.d.l. - below detection limit

* Fe_{tot} calculated as Fe^{3+}

** H_2O calculated from charge balance (in Ves), and from Si deficiency at tetrahedral position (in Grt)

Table 3 Selected trace element concentrations (ppm) in vesuvianites and garnets. Additional analyses are available in Table S2.

	Ves I			Ves II			Grt I			Grt II		
Rb	-	-	0.018	0.016	-	-	-	0.008	0.018	0.130	-	0.055
Ba	1.190	0.500	1.800	0.200	-	0.524	0.332	0.180	1.040	-	0.860	-
Th	0.002	0.006	-	-	0.001	-	-	0.005	0.004	-	0.014	-
U	0.008	0.003	0.002	0.011	0.106	0.004	0.000	0.001	0.001	0.002	-	0.003
Nb	0.215	0.101	0.147	0.036	0.012	1.130	1.193	1.300	1.780	0.188	0.203	0.230
Ta	0.040	-	0.026	0.009	-	0.059	0.077	0.083	0.094	0.004	-	0.005
La	1.650	0.186	1.100	1.150	12.320	0.453	0.037	0.173	0.119	-	0.200	-
Ce	4.630	0.520	2.810	2.920	43.650	0.807	0.093	0.374	0.295	-	-	0.018
Pb	1.490	0.243	1.240	0.148	0.017	0.417	0.345	0.080	0.520	0.400	0.210	0.036
Pr	0.640	0.062	0.530	0.460	5.650	0.082	0.015	0.038	0.033	0.021	0.066	0.006
Sr	58.640	183.280	14.580	87.300	61.970	118.470	0.339	7.370	1.870	-	-	0.116
Nd	3.370	0.470	2.740	3.050	22.410	0.400	0.081	0.308	0.154	-	0.120	0.084
Zr	31.180	3.480	23.210	1.530	0.701	238.640	226.800	131.540	111.930	113.270	104.970	111.250
Hf	0.474	0.127	0.840	0.010	0.020	4.920	10.410	4.420	4.140	3.840	3.940	4.120
Sm	1.580	0.175	1.470	1.870	4.400	0.061	0.094	0.168	0.071	0.360	0.210	0.096
Eu	1.360	0.331	1.310	1.540	3.730	0.139	0.045	0.172	0.097	0.171	0.550	0.363
Gd	2.310	0.640	1.890	3.480	3.830	0.082	0.248	0.680	0.620	-	1.280	0.370
Dy	2.060	0.940	2.620	5.180	4.320	0.100	1.070	2.590	3.180	1.340	2.330	1.050
Ho	0.552	0.249	0.460	1.120	0.929	0.023	0.388	0.900	1.310	0.300	0.790	0.204
Er	1.380	0.860	1.730	3.080	2.520	0.085	1.590	3.420	5.490	1.040	2.580	0.800
Yb	1.580	1.090	1.970	2.790	2.340	0.153	2.440	5.900	9.460	1.780	4.120	1.740
Y	14.630	8.170	16.890	30.570	23.950	0.851	11.310	20.730	28.680	11.120	24.310	8.760
Lu	0.297	0.141	0.300	0.339	0.305	0.035	0.390	1.050	1.630	0.459	0.640	0.276

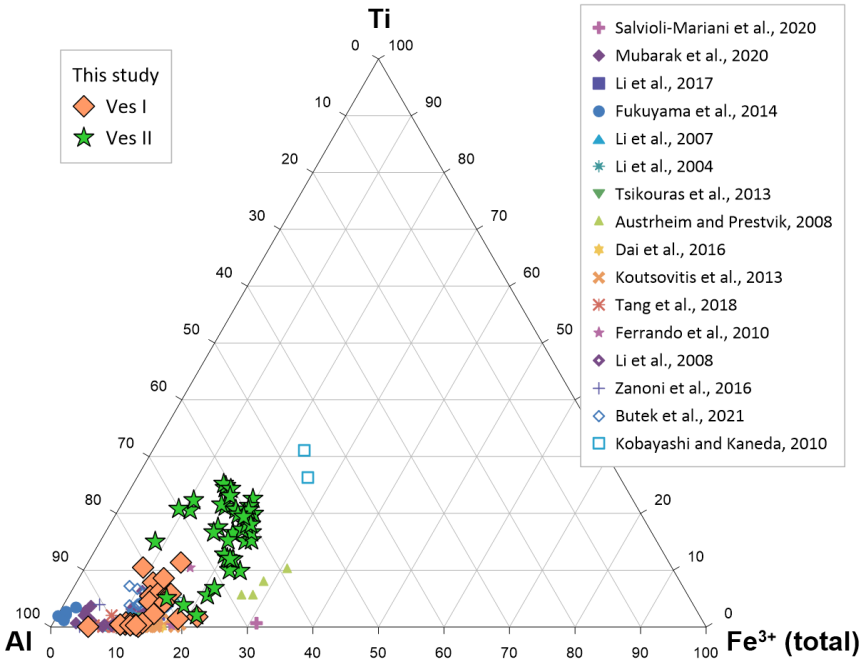

Figure 5 Al-Ti-Fe3+ ternary diagram of the chemical composition in vesuvianites from the Bôrček locality. The compilation of vesuvianite data from various rodingites is added for comparison (note that an appropriate distinction between vesuvianite and garnet was not always performed in the available studies and thus the dataset possibly contain some misidentifications of those two minerals).

Garnet solid solution dominantly belongs to grossular-andradite series and it is, similarly to vesuvianite, characterized by significant composition heterogeneity with very variable contents of major elements, mainly Al, Fe, and Ti (Fig. 8, 9a-c). Compared to the composition of vesuvianite, garnet has a generally higher Fe/Al ratio and it contains almost no MgO (≤ 0.5 wt.%). The andradite end-member represents the most dominant component in all analyses, but grossular, Ti-garnet, and even a hydrated end-member appears in the garnet solid solution (Tab. 2). There is a notable compositional difference between garnet I and garnet II. Although the Al/Fe (Grs/Adr) variation is very similar in both garnet types (Fig. 8), garnet II is clearly enriched in TiO_2 (1.2 – 5.6 wt.% compared to 0.2 – 1.6 wt.% in garnet I) and its OH content is also more significant (H_2O = 0.2 – 2 wt.% compared to 0 – 0.9 in garnet I). The average structural formula of garnet I and garnet II considering all iron to be Fe^{3+} can be expressed as $Ca_{2.99}$ $(Fe^{3+}_{1.30}Al_{0.63}Ti_{0.05}Mn_{0.02}Mg_{0.01})_{\Sigma 2.01}$ $Si_{2.94}$ $\square_{0.06}$ $O_{12.01}$ and as $Ca_{2.98}$ $(Fe^{3+}_{1.28}Al_{0.46}Ti_{0.23}Mn_{0.02}Mg_{0.03}V_{0.01})_{\Sigma 2.03}$ $Si_{2.84}$ $\square_{0.16}$ $O_{12.1}$, respectively; the empty box denotes vacancy from which the OH content was calculated. Electron microprobe composition maps document the complex composition variations and show that garnet tends to be Al-richer in the inner parts of the rims around oxide minerals (Fig. 9a-c, Fig. S4) but equally Al-richer at the contact with epidote (Fig. 9d, e; Fig. S5).

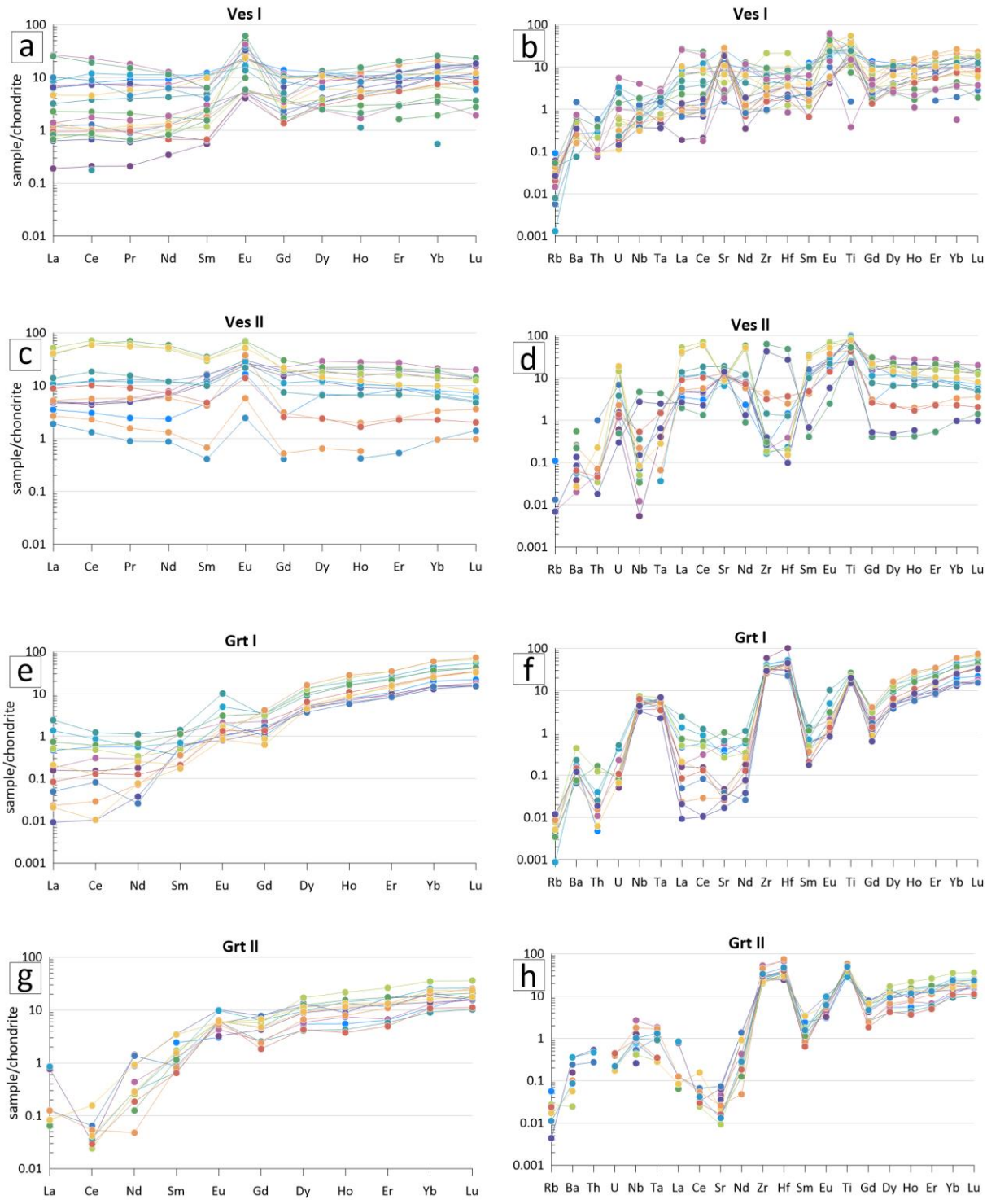

Figure 6 Chondrite-normalized REE and trace element spider diagrams for the different vesuvianite and garnet generations (chondrite values from McDonough and Sun 1995). Each pattern represents a single LA-ICP-MS analysis (Table S2).

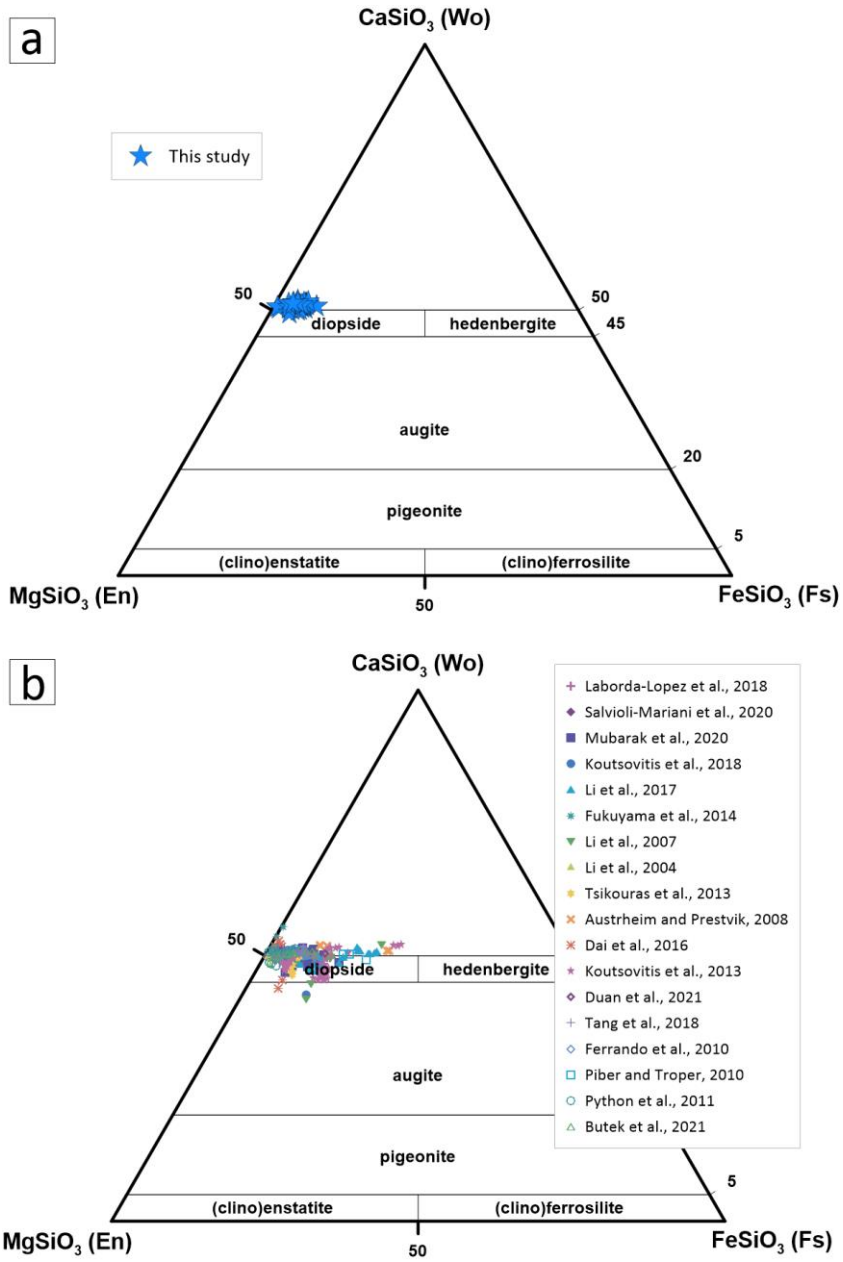

Figure 7 Ternary classification diagram for the studied clinopyroxenes (after Morimoto 1988). a) Clinopyroxenes from this study. b) Compilation of hydrothermal clinopyroxene data from various rodingites for comparison.

The REE patterns of garnets show an increasing trend with distinct depletion of LREE and enrichment of HREE relative to chondrite values (Fig. 6e, g; Tab. 3). Similarly to vesuvianite, both garnet types feature a consistent but less pronounced positive Eu anomaly. Trace element concentrations in both garnet types are fairly coherent and demonstrate Rb depletion, Nb, Ta enrichment and significantly high Zr, Hf, and Ti reaching 30-50 times chondrite values (Fig. 6f, h). Slight differences occur between garnet I and garnet II. The enrichment of Nb and Ta is lower in garnet II. Garnet II shows a more significant Ti enrichment than garnet I, which is consistent with major oxide chemistry determined by electron microprobe measurements. Garnet I displays a larger range of La, Ce, and Sr concentrations than garnet II.

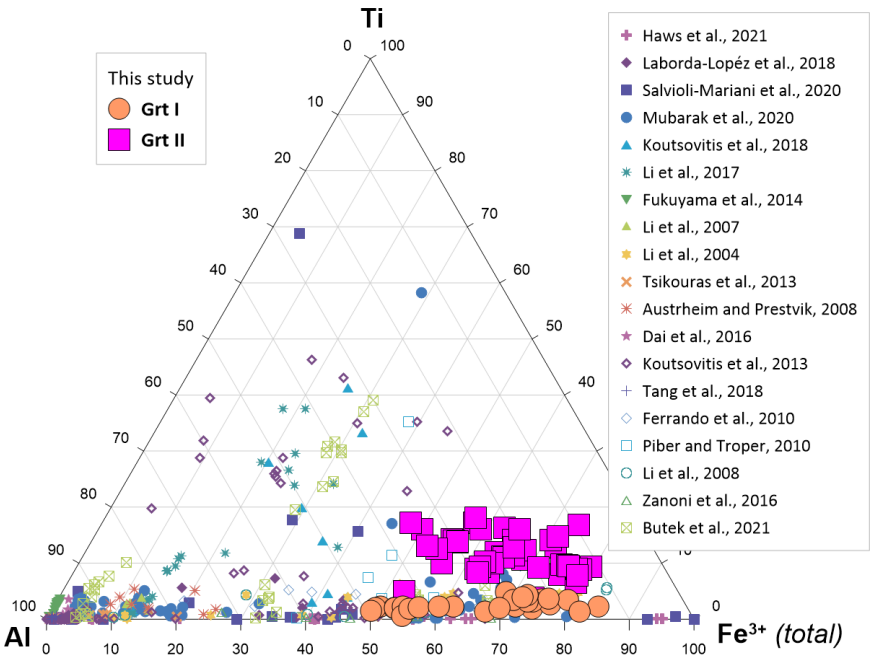

Figure 8 Al-Ti-Fe ternary diagram of the chemical composition in investigated garnets. The Al/Fe (grossular/andradite) variation is similar in both generations; however, garnet II is clearly enriched with Ti. The compilation of garnet data from various rodingites is added for comparison (note that an appropriate distinction between garnet and vesuvianite was not performed in the available studies and thus the dataset possibly contain some misidentifications of these two minerals).

Titanite composition is characterized by low Al_2O_3 and FeO contents (< 1.9 wt.% and < 1.5 wt.%, respectively) and high TiO_2 content (37.4 – 40 wt.%). The average structural formula of titanite can be written as $Ca_{1.00}Ti_{0.94}Al_{0.04}Fe^{3+}_{0.02}V_{0.01}Si_{0.99}O_{4.97}$.

Epidote composition is homogeneous with major oxides not exceeding variations of 1 wt.%. Its simplified average structural formula can be expressed as $Ca_{2.02}Al_{2.30}Fe^{3+}_{0.65}Mg_{0.01}Si_{3.01}O_{11.99}(OH)_1$ and can therefore be classified as epidote sensu stricto (Armbruster et al., 2006).

Chlorite shows a high MgO content (> 29 wt.%) and a significant variation in Al_2O_3 (15.3 – 21.3 wt.%). The average chlorite formula can be expressed as $Mg_{4.33}Fe^{2+}_{0.49}Al_{1.10}Si_{3.00}Al_{1.00}O_{10}(OH)_8$ ($Clc_{89.7}Chm_{10.1}Pnn_{0.2}$). Therefore, all analyzed chlorites can be classified as clinochlores (Yavuz et al., 2015). No systematic differences in the chemical composition were identified with respect to chlorite type (I-III). Chlorites do not accumulate a significant amount of trace elements.

Carbonate minerals are virtually pure calcite, but slight but significant compositional variations are observed between calcite II and calcite III. Calcite II shows a composition of $Ca_{0.996}Mg_{0.003}Fe_{0.001}$, while Cal III, forming late veins, is even more pure with average $Ca_{0.999}Mg_{0.001}$. Except the expected high amount of Sr, calcite does not contain any significant amount of other trace elements.

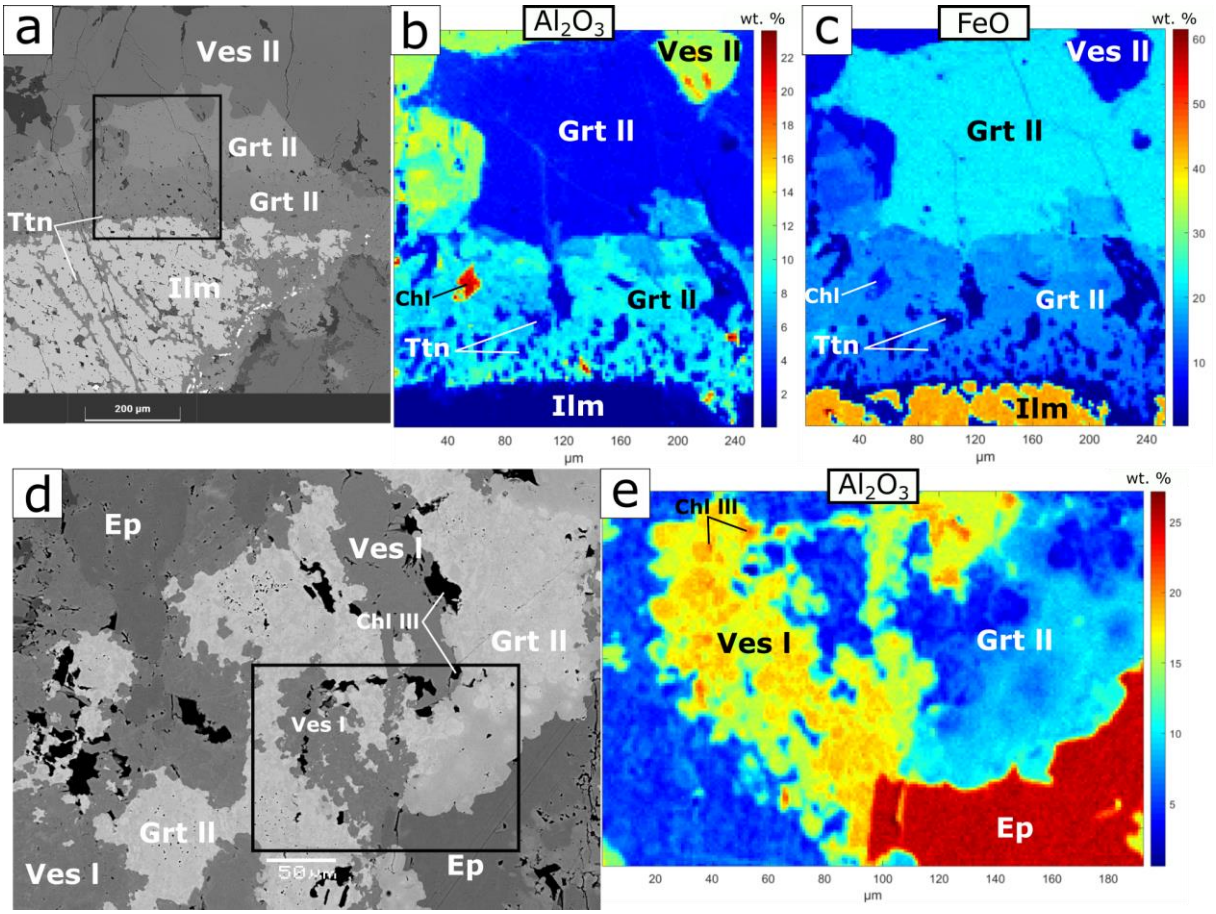

Figure 9 Electron microprobe chemical composition maps. a) BSE image showing the garnet II + titanite association as a rim around an ilmenite crystal (sample FBR-55). The black rectangle delimits the mapped area. b), c) Al_2O_3 and FeO, respectively. Note the Al/Fe heterogeneity in the garnet. d) BSE image showing vesuvianite I + garnet II surrounded by epidote (sample FBR-55). The black rectangle delimits the mapped area. e) Al_2O_3. Note that the proximity of homogeneous epidote shifts the garnet composition to the grossular end-member. Complementary element maps can be found in Figures S3-S5. Mineral abbreviations are after (Whitney and Evans 2010).

4.3 Whole rock composition

The whole rock composition of rodingites is characterized by high CaO (21.7 – 29.3 wt.%), low SiO_2 (30.8 – 38.3 wt.%) and they are completely devoid of Na and K (Tab. 4). Other major oxides display even more variable values: Al_2O_3 (7.3 – 16.4 wt.%), Fe_2O_3 (3.7 – 12.8 wt.%), FeO (0.5 – 2.9 wt.%) and MgO (5 – 11 wt.%). The TiO_2 content allows to accordingly classify the investigated samples into Ti-rich (5.16 – 9.26 wt.% TiO_2; FBR-55, FBR-56, FBR-57 and FBR-64) and rather ordinary Ti-poor (0.59 – 1.02 wt.% TiO_2; FBR-61, FBR-63 and FBR-70) rodingites (Fig. 10) which is consistent with the presence or absence of Fe-Ti oxides. Interestingly, Fe and Ti enrichments are not correlated. The Fe^{3+}/Fe_{tot} ratio is slightly lower in oxide-rich samples due to the presence of Fe^{2+} in ilmenite and it varies from 0.6 to 0.73. LOI values vary from 3.3 to 7.7 wt.%.

Table 4 Whole rock composition of analyzed rodingite samples. Major oxides, LOI, TOT/C and TOT/S values are in wt.%. Trace elements values are in ppm.

sample	FBR-55	FBR-56	FBR-57	FBR-61	FBR-63	FBR-64	FBR-70
SiO_2	31.81	30.84	38.27	35.09	37.62	37.8	33.52
TiO_2	5.16	9.26	7.07	0.59	0.76	5.95	1.02
Al_2O_3	11.74	7.27	7.9	16.41	13.94	9.61	15.1
Cr_2O_3	0.007	0.012	0.014	0.012	0.021	0.012	0.07
Fe_2O_3	10.05	12.82	5.06	3.67	3.84	4.30	7.24
FeO	2.63	2.88	0.86	0.55	0.59	0.79	1.97
MnO	0.17	0.24	0.14	0.11	0.11	0.11	0.14
MgO	7.03	4.95	8.27	9.61	10.46	8.09	10.99
CaO	24.92	26.3	28.68	27.96	27.66	29.34	21.74
Na_2O	<0.01	<0.01	<0.01	<0.01	<0.01	<0.01	<0.01
K_2O	<0.01	<0.01	<0.01	<0.01	<0.01	<0.01	<0.01
P_2O_5	0.32	0.07	<0.01	<0.01	<0.01	<0.01	<0.01
LOI	5.5	4.7	3.3	5.7	4.7	3.5	7.7
Sum	99.68	99.66	99.68	99.79	99.75	99.68	99.71
Ba	16	10	4	6	5	5	5
Ni	173	117	224	130	138	237	255
Sc	39	66	64	32	55	45	36
Be	3	<1	<1	<1	3	<1	<1
Co	40.3	28.7	22.5	23.3	25.2	24.6	51.4
Cs	<0.1	<0.1	<0.1	<0.1	0.1	0.1	<0.1
Ga	5.9	4.5	3	3.4	4.3	4.4	5.8
Hf	6.4	5.3	1.9	1.4	0.3	0.7	0.8
Nb	5.3	6.2	1.7	1.2	<0.1	<0.1	<0,1
Rb	0.7	0.1	0.2	0.2	0.2	0.4	0.4
Sn	2	2	<1	<1	<1	<1	<1
Sr	195.2	192.6	42.4	40.9	34.1	20.6	240.7
Ta	0.4	0.5	0.1	<0.1	<0.1	<0.1	<0.1
Th	<0.2	<0.2	<0.2	<0.2	<0.2	<0.2	<0.2
U	0.8	0.5	0.5	0.2	0.2	0.4	0.3
V	538	950	811	860	179	289	306
W	6	17.2	9.4	8.7	2.6	3.9	2.9
Zr	251.3	190.2	58.6	46.6	9.6	15.3	22.8
Y	56.1	37.5	26.4	17.4	9.3	17	13.8
La	7.2	2.1	4.8	1.9	0.8	1.5	0.9
Ce	23.1	7.4	15.5	5.1	1.2	1.8	2.1
Pr	3.99	1.45	2.38	0.79	0.23	0.39	0.42
Nd	21.5	9.2	10.3	4.2	1.6	3	2.8
Sm	6.99	3.52	2.97	1.53	0.7	1.27	1.17
Eu	2.68	1.47	2.39	1.24	0.53	0.61	0.56
Gd	9.32	5.4	4.17	2.47	1.18	2.27	1.88
Tb	1.61	1.01	0.74	0.44	0.23	0.43	0.35
Dy	9.83	6.51	4.87	2.91	1.56	2.91	2.5
Ho	2.14	1.55	1.12	0.61	0.35	0.69	0.52
Er	6.32	4.47	3.16	1.84	1.14	1.96	1.64
Tm	0.83	0.61	0.44	0.27	0.15	0.27	0.21
Yb	5.3	3.95	2.93	1.73	1.02	1.76	1.34
Lu	0.84	0.63	0.47	0.27	0.16	0.26	0.2
TOT/C	0.67	0.75	0.26	0.23	0.13	0.07	0.82
TOT/S	<0.02	<0.02	0.03	<0.02	<0.02	<0.02	<0.02

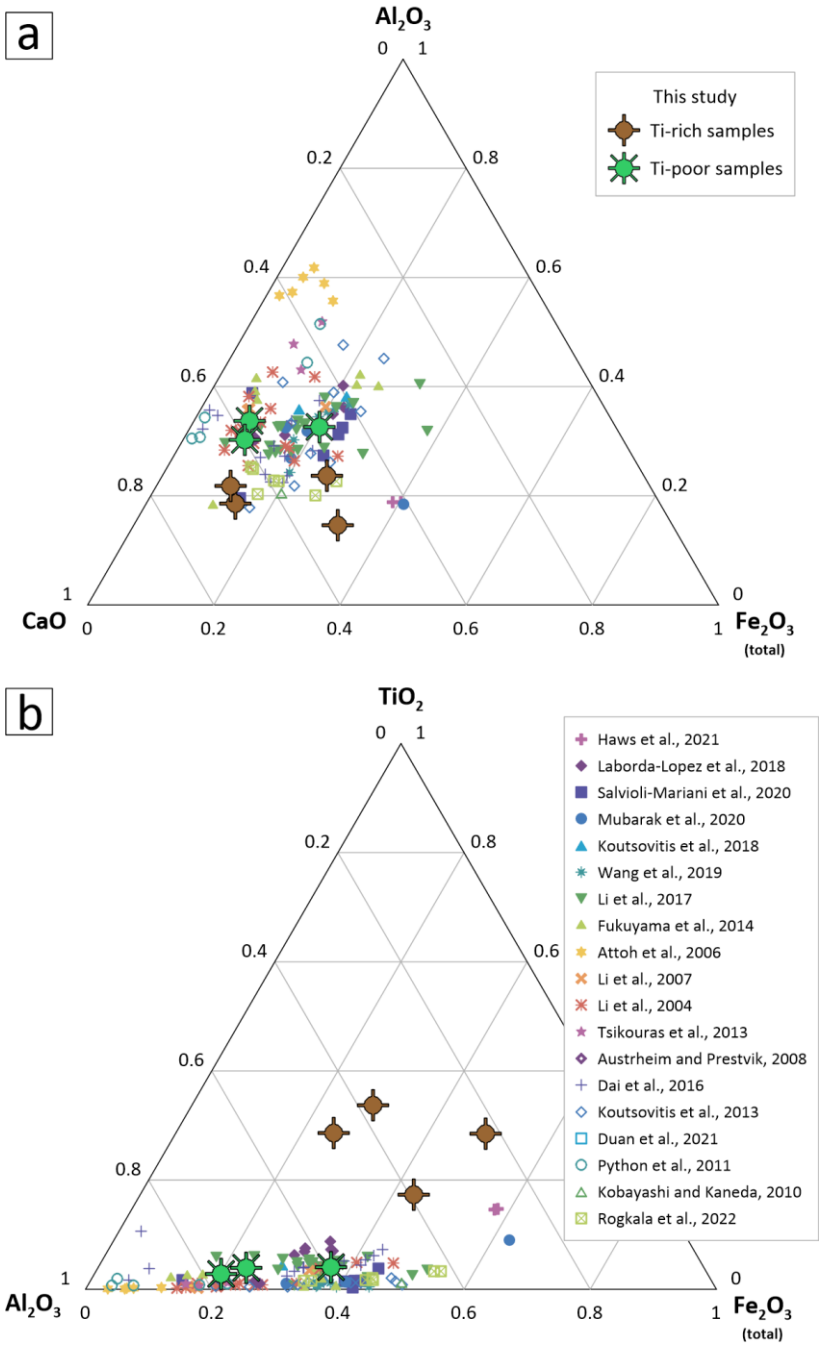

Figure 10 Ternary diagrams of the rodingite whole rock composition. a) CaO-Al_2O_3-Fe_2O_3 diagram. Compilation of whole rock data of rodingites from various other localities is shown for comparison. Samples with LOI exceeding 8 wt.% were excluded from the dataset. b) Al_2O_3-TiO_2-Fe_2O_3 diagram. Ti enrichment is particular for the rodingites from this study.

The REE whole rock patterns display an enrichment relative to chondrite (Fig. 11a). However, the degree of enrichment is fairly variable. Ti-rich samples generally contain more REE than Ti-poor samples (Σ_{REE} = 19 – 102 ppm compared to 11 – 25 ppm). The patterns are relatively flat or slightly LREE-depleted. A clear positive Eu anomaly is observed only in 3 samples, while other patterns show basically no Eu anomaly. This Eu positive anomaly and the lack of such anomaly in the 4 others suggest a variation of the plagioclase modal content in the protolith of the investigated rodingites.

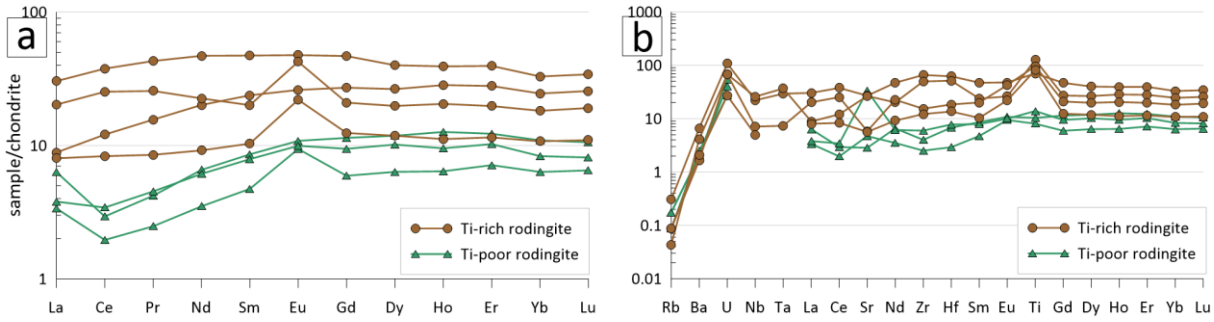

Figure 11 Chondrite-normalized REE and trace elements spider diagrams for whole rock rodingite analyses (chondrite values from McDonough and Sun 1995). Each pattern represents a single sample.

The spider diagram of trace elements displays a Rb depletion, noticeable positive U anomaly, and variable Sr content (Fig. 11b). The enrichment of high-field-strength elements such as Nb, Ta, Zr, and Hf is more significant in Ti-rich samples. Two Ti-rich rodingites samples (FBR-57, FBR-64) have significantly lower Fe and Mn content when compared to the two other investigated samples of the same type (Fig. S6, S7). Considering that ilmenite contain more iron (and Mn) than rutile or titanite, we suggest that this results from a variation of the ilmenite/rutile/titanite modal ratio. Those samples are also characterized by lower Zr, Hf, Nb and Ta (Fig. S8, S9), contrary to the two others. The variation in HFSE among samples could be related to the variation of the modal abundance of rutile itself as that mineral tends to incorporate preferentially those elements when compared to ilmenite (e.g. Lorand and Gregoire, 2010).

5 Discussion

5.1 Primary minerals and protolith of rodingites

The most frequently described protoliths for rodingites worldwide are mafic dykes, especially dykes of gabbroic/diabase rocks (e.g. Koutsovitis, 2017; Li et al., 2017), but rodingites can also rarely derive from other types of rocks such as slate or quartzite (e.g. El-Shazly and Al-Belushi, 2004; Normand and Williams-Jones, 2007). Since the rodingites from Bôrček were sampled from dumps, field relationships can not help to identify their protolith. However, their petrological and geochemical characteristics together with the context of occurrence allow to discuss the original rock.

Textural observations show that clinopyroxene is commonly rimmed by garnet (Fig. 3f, g; Fig. 4d), enclosed in epidote (Fig. 3j, Fig. 4j), replaced by vesuvianite and chlorite (Fig. 4e) and crosscut by numerous veins filled in particular by either vesuvianite (Fig. 3e) or garnet (Fig. 3g). It is thus interpreted as the oldest mineral phase. It displays exsolution lamellae (Fig. 4e) but the latter is not an evidence of a magmatic origin but of subsolidus equilibration. Moreover the crystals are xenomorphic and show intense marks of internal deformation including ondulatory extinction (Fig. 3e) and subgrains (Fig. 3b), sometimes leading to recrystallization of small grains (Fig. 3e). Chemical analysis by LA-ICPMS allow to further discuss its magmatic versus metamorphic origin. Magmatic clinopyroxene generally accumulates the most significant quantities of REE in ultramafic to mafic rocks. However, all analyzed clinopyroxenes from Bôrček are chemically homogeneous and characterized by very low trace element concentrations. They are also lower in Al_2O_3, FeO, and relatively rich in CaO compared to pyroxenes of magmatic origin (e.g. Barriga and Fyfe, 1983). Furthermore, the Mg# values

of the diopsides are too high (up to 96) to originate from magma crystallization (Nishiyama et al., 2017; Python et al., 2007) and are in good agreement with hydrothermal diopsides reported in the literature (Fig. 12). All these features allow us to conclude that clinopyroxenes from investigated rodingites are related to a single hydrothermal event and that no relic of magmatic clinopyroxene is preserved.

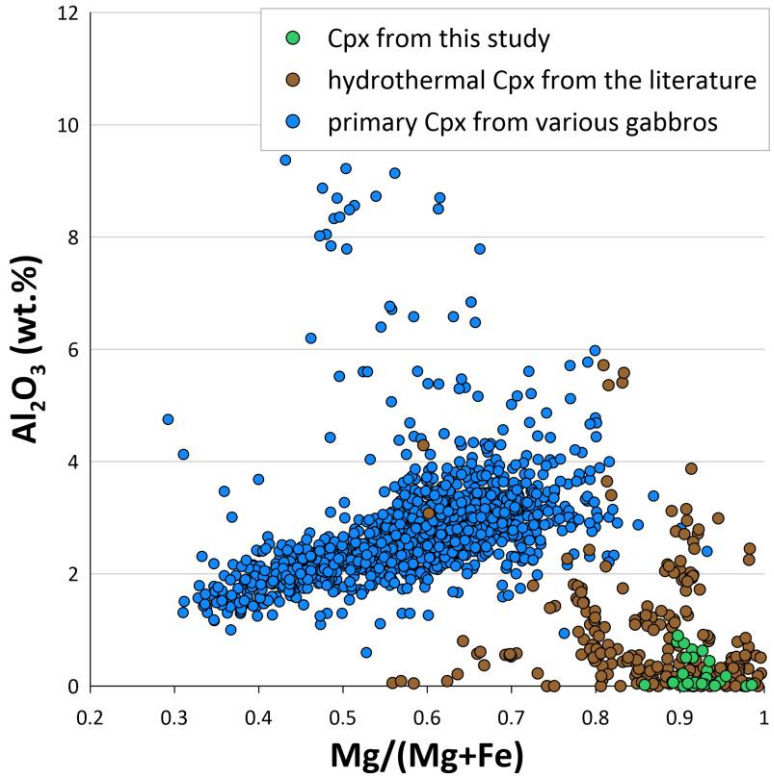

Figure 12 Al_2O_3 versus Mg# of the studied diopsides compared to secondary clinopyroxenes in rodingites from the literature (the same dataset as in Figure 7). Chemical compositions of magmatic clinopyroxenes from various gabbroic rocks are added to disciminate magmatic and hydrothermal origin. The data for magmatic clinopyroxenes were downloaded from the PetDB Database (www.earthchem.org/petdb) on 7, September 2022, using the following parameters: rock type = gabbro, mineral = clinopyroxene.

The geochemical signature of vesuvianite as the dominant phase in studied rodingites is characterized by high Al_2O_3 contents (cf. Groat et al., 1992), mainly in the case of vesuvianites of the first generation (14 – 19.8 wt.%). Moreover, the majority of vesuvianites of both types display decreasing REE patterns and significant positive Eu anomaly, which resemble those of unaltered plagioclase (cf. Lesnov, 2010). Consequently, we propose that the vesuvianite derives at least partially from the transformation of plagioclase during the rodingitization processes.

The TiO_2 whole rock content in rodingites around the world rarely exceeds 2 wt.%. The most significant content (5.2 wt.%) was recently reported by Haws et al. (2021) in metarodingites formed by subduction of metasomatized (Fe-Ti) gabbro from the Voltri Unit (Western Alps). The Ti-rich rodingites described in the present study are characterized by a TiO_2 content ranging from 5 up to 9 wt.% which represents the highest Ti values in rodingitized rocks reported so far.

TiO_2 and Al_2O_3 are typically considered as the least mobile major elements during hydrothermal alteration processes and we will assume in the following their low mobility during the formation of rodingites at Bôrček. We observe that the measured whole rock concentrations compare well with compositions of a variety of gabbroic rocks (Fig. 13). Furthermore, whole rock REE normalized spectra (Fig. 11) characterized by variable Eu anomaly and higher REE concentrations in Ti-rich samples are in good agreement with values reported from gabbroic rocks in Alpine ophiolites (cf. McCarthy and Müntener, 2019). Based on major and REE characteristics, we distinguish two types of protolith. We suggest that Ti-poor rodingites (samples FRB-61, FBR-63 and FBR-70) which are characterized by low Fe-Ti contents [$(Fe_2O_3+TiO_2)_{WR}$ < 5.3 wt.%], higher Mg# (0.82) and low REE contents derive from a gabbroic protolith with a common magnesian composition. On the other hand, Ti-rich rodingites (samples FBR-55, FBR-56, FBR-57 and FBR-64) with $(Fe_2O_3+TiO_2)_{WR}$ > 10 wt.%, Mg# < 0.76 and high REE contents derive from a magmatically more differentiated oxide-rich (Fe-Ti) gabbroic rock.

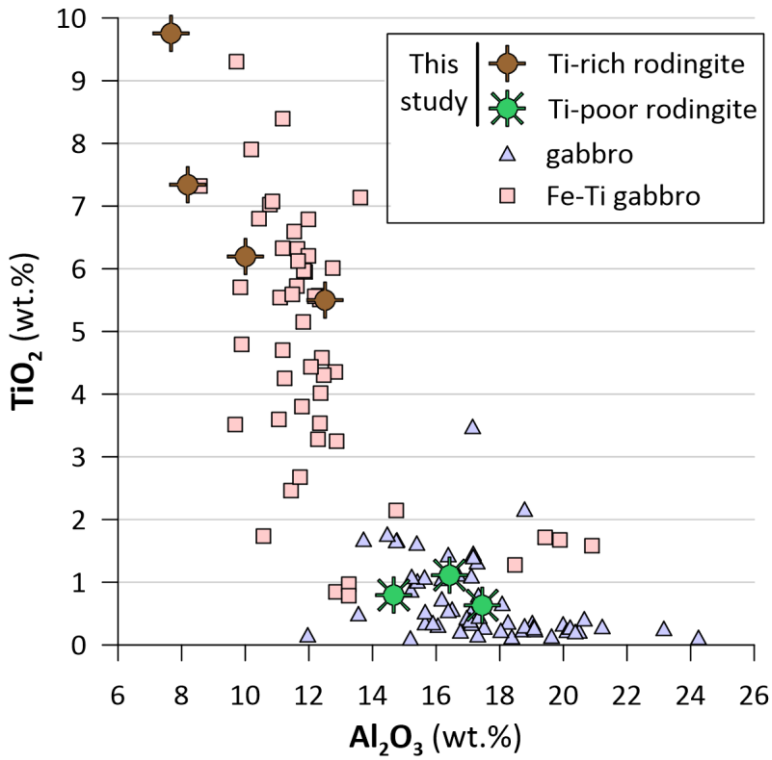

Figure 13 TiO_2 versus Al_2O_3 diagram comparing the whole rock composition of studied rodingites with proposed types of gabbroic protolith. Data for common magnesian (meta)gabbro (Schwartz et al. 2000; Montanini et al. 2006; Miller et al. 2007; Bucher and Grapes 2009; Bucher and Stober 2021) and Fe-Ti (meta)gabbro (Liou et al. 1998; Schwartz et al. 2000; Montanini et al. 2006; McCarthy and Müntener 2019; Starr et al. 2020) are from ophiolite occurrences from the Alpine-Apennine orogenic belt. All data were recalculated on anhydrous basis in wt.%. Assuming restricted mobility of Ti and Al during metasomatic and/or metamorphic process, we infer a common gabbro as protolith for the Ti-poor samples and a Fe-Ti gabbro for the Ti-rich rodingites from Bôrček.

The association of magnesian gabbroic rocks and Fe-Ti gabbroic rocks is reminiscent of what we observe in present-day ocean floor (e.g. MacLeod et al., 2017), but also in some (meta-)ophiolites affected by less intense processes of serpentinization and rodingitization (e.g.

Bocchio et al., 2000; McCarthy and Müntener, 2019). The obducted oceanic lithosphere observed in the Alpine-Apennine ophiolites is typically considered to originate in a slow spreading ocean ridge. Despite the fact that unaltered gabbroic rocks were not described in the Western Carpathians, the close spatial relationship of the investigated samples to the serpentinized rock, which presumably derived from a mantle peridotite (Hovorka et al., 1985), suggests a probable presence of a similar ophiolitic rock association at Bôrček as well.

5.2 Evolution of mineral parageneses

Despite the intricate mineral relationships, textural observations allow to determine the formation succession of metasomatic minerals. Considering the Fe-Ti gabbroic protolith for Ti-rich samples, we propose that Fe-Ti oxides (ilmenite and possibly rutile) together with scarce sulfide minerals are at least partially inherited from the igneous protolith (Fig. 14a). On the contrary, typical primary minerals of the gabbroic rock, such as pyroxene and plagioclase, were consumed and completely replaced by new rodingitic assemblage(s).

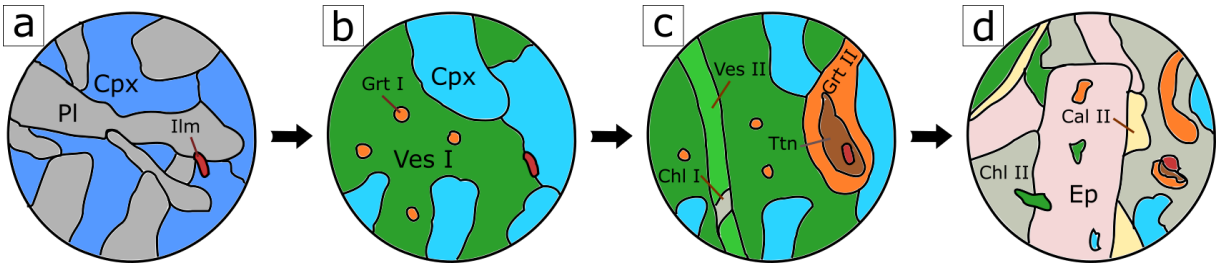

Figure 14 Sketch illustrating the model evolution of mineral parageneses in rodingites from Bôrček. a) Initial magmatic stage (gabbroic protolith) characterized by mineral assemblage of plagioclase, pyroxene and Fe-Ti oxides (ilmenite and/or rutile). b) First stage of rodingitization characterized by the formation of vesuvianite I, clinopyroxene and garnet I. c) Second stage of rodingitization characterized by the destabilization of Fe-Ti oxides and the formation of titanite, garnet II and veinlets filled with vesuvianite II and chlorite I. d) Hydrothermal alteration represented by the crystallization of epidote, chlorite II and calcite II. The very late formation of carbonate veins (calcite III) is not shown in the figure.

The first metasomatic process is characterized by crystallization of the mineral association vesuvianite I + diopside ± garnet I (Fig. 14b), and represents therefore a first rodingitization event. Vesuvianite I represents the dominant phase in almost all samples and as a whole, this first mineral assemblage represents at least 75 % of the mineral mode. The prevailing presence of vesuvianite is often regarded as evidence of a high extent of Ca metasomatic transformation (Ferrando et al., 2010; Li et al., 2004; Schandl et al., 1989) which is consistent with the fact that no major primary (igneous) mineral was identified in the investigated rodingites.

The second stage of the hydrothermal transformation is characterized by crystallization of the association garnet II + titanite + vesuvianite II ± chlorite I (Fig. 14c) and thus represents a second rodingitization event. The occurrence of garnet II and titanite is generally linked to oxide aggregates. The textural observations showing widespread pervasive titanite enclosing ilmenite and rutile (Fig. 4g, i) and high Ti contents in vesuvianite II and garnet II suggest that the destabilization of ilmenite and rutile supplied Ti that was then incorporated into titanite and newly formed garnet and vesuvianite. The chemical composition of titanite (high Ti; low Al, Mg, Fe) also demonstrates its metamorphic origin induced by ilmenite destabilization

(Mohammad and Maekawa, 2008). Interestingly, the Ti-rich vesuvianite II (up to 7.3 wt.% TiO_2; 2.7 Ti apfu) occurring in the veins investigated in the present study represents one of the most titaniferous vesuvianite reported worldwide (cf. Aksenov et al., 2016; Kobayashi and Kaneda, 2010). During this second stage, widespread fracturing resulted in a complex vein system filled dominantly with vesuvianite II ± chlorite I. As vesuvianite II is generally related to the occurrence of vesuvianite I, it seems that vein filling is more likely influenced by the surrounding mineral and rock composition at the millimetric scale. Therefore, the chemical composition of the involved hydrothermal fluid does not represent the most important factor controlling the mineral assemblage in the vein. Several reports of vesuvianite-dominated veinlets exist in the literature (Bidyananda et al., 2021; Ferrando et al., 2010; Li et al., 2008; Normand and Williams-Jones, 2007), however, their origin and relationships to the earlier generation of vesuvianite were not examined in much detail.

The third distinct hydrothermal event is evidenced by the crystallization of the association epidote + chlorite II ± calcite II (Fig. 14d). The presence of numerous relics of vesuvianite, garnet and diopside enclosed in this well crystallized association (Fig. 4j), suggests a direct replacement of the first metasomatic paragenesis. This hydrothermal alteration is very unevenly distributed and in some samples, epidote was not identified at all (Tab. 1). This suggests that the transformation was controlled by channeled fluid circulation near faults and fractures where a higher volume of fluid flowed. Epidote-group minerals usually represent common rodingite minerals mainly in samples that were only slightly affected by the rodingitization process (Duan et al., 2021; Li et al., 2004; Schandl et al., 1989). This is why epidote is often considered to be one of the first rodingite minerals to form. However, epidote also represents a typical product of widespread metamorphism under relatively low P-T conditions. We suggest that in the case of rodingites from Bôrček, the formation of a late association epidote + chlorite ± calcite II is not related to the rodingitization process but to the later regional metamorphism in greenschist facies conditions and the subsequent exhumation process. Similar interpretation of epidote occurrence was inferred from metarodingites from the Central Alps by Evans et al. (1981).

The latest process transforming the investigated rodingites is characterized by numerous calcite veinlets (calcite III) formed during CO_2-rich fluid infiltration which affected also the adjacent serpentinite. This late CO_2-rich fluid sporadically provoked recrystallization and formation of sub- to euhedral garnet and titanite crystals on the edge of calcite veins (Fig. 3i).

5.3 Element mobility during hydrothermal alteration

The observed mineral evolution and chemical compositions allow to discuss element mobility during the hydrothermal alteration leading to the rodingite formation. Chemical composition of the investigated samples is in good agreement with rodingite compositions reported in the literature (Fig. 15), in particular with respect to SiO_2 and CaO content. Silica leaching and Ca enrichment define a rodingitization trend from non-altered rocks (chemically similar to gabbroic protoliths; $37 < SiO_2 < 52$ wt.%; $6 < CaO < 16$ wt.%) to intensively rodingitized rocks characterized by low SiO_2 (35 – 40 wt.%) and high CaO (up to 38 wt.%) contents. The evolving concentrations of SiO_2 and CaO is thus taken as a proxy for the extent of rodingitization process (Duan et al., 2022; Laborda-López et al., 2020; Rogkala et al., 2022). We conclude from the low SiO_2 (32 – 40 wt.%) and high CaO (23 – 31 wt.%) content of the rodingites from Bôrček that they represent very intensively metasomatized rocks. Two Ti-rich samples (FBR-55 and FBR-56) even display the lowest Si content reported so far in rodingitic samples. The

assumption of the intense metasomatic process is also supported by the complete removal of the alkali elements Na and K. All these chemical changes suggest an open hydrothermal system and are in good agreement with the globally accepted concept of rodingite formation (Koutsovitis et al., 2013; Laborda-López et al., 2020; Li et al., 2017, 2007; Tang et al., 2018).

The Al/Fe variations (Fig. 8) together with slight Mn differences in both garnet generations are spatially related to the late epidote-chlorite-calcite assemblage, with FeO decrease and Al_2O_3 increase in the vicinity of the epidote (Fig. 9e, and S4c, d). Investigated epidotes are very homogeneous in composition and contains about 10.8 wt.% Fe_2O_3. We suggest that iron was partially leached from garnet by the epidote forming fluid, thus leading to an increase of the Al/Fe ratio in surrounding garnet. A similar relationship between garnet and epidote was also proposed by Schulte and Sindern (2002).

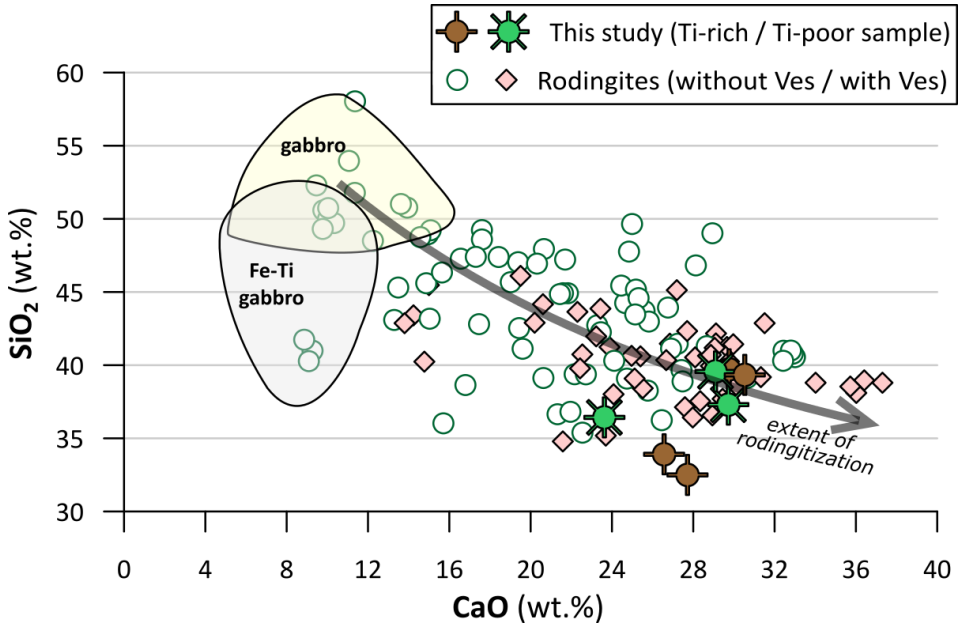

Figure 15 SiO_2 versus CaO diagram illustrating the rodingitization progress by Si leaching and Ca enrichment. Whole rock compositions of rodingites from the literature (same as in Figure 10) are plotted and classified according to vesuvianite absence or presence. Fields for common and Fe-Ti (meta)gabbros are drawn using a dataset from ophiolite occurrences in the Alpine-Apennine orogenic belt (Liou et al. 1998; Schwartz et al. 2000; Montanini et al. 2006; Miller et al. 2007; Bucher and Grapes 2009; Starr et al. 2020; Bucher and Stober 2021). All data were recalculated on anhydrous basis in wt.%. Whole rock compositions and high modal amounts of vesuvianite reported in this study are in good agreement with an intense metasomatic process.

Titanium mobility can be significant in highly alkaline fluid but its mobility decreases with increasing pressure and titanium is generally considered as immobile during fluid-rock interactions, in particular in subduction zone environments (Tsikouras et al., 2013 and references therein). In our samples, titanium immobility at the sample scale is supported by the fact that whole rock concentrations in the Al_2O_3-TiO_2 diagram are consistent with the composition of a gabbroic protolith (Fig. 13). However, both second generations of vesuvianite and garnet document significant Ti enrichment (Fig. 5, 8) compared to the first generation. Interestingly, several studies describe a chemical zonation in vesuvianite (from core to rim, Ferrando et al., 2010; or from a first generation of vesuvianite to a second one, Kobayashi and

Kaneda 2010; Zanoni et al. 2016) with decreasing Ti content (and increasing Al), the opposite of the observation reported in this study. Similarly, a higher Ti content was observed in earlier crystallized (older) garnet in rodingites described by Laborda-López et al. (2018), which again differs from our observations. Li et al. (2007) suggested that Ti can be leached out from the protolith during intense rodingitization; however, the intense metasomatism and high TiO_2 reported in our study show that Ti content in rodingites is controlled by the chemical composition of protolith, not by the extent of Ca-metasomatism (Fig. 13). Despite the fact that some authors suggested considerable Ti mobility and the addition of this element from an external source into the rodingite during its formation (Austrheim and Prestvik, 2008; Piber and Tropper, 2010), in our case, we rather suggest that Ti is mobile only at the mineral scale and assume an internal source of Ti generated by ilmenite and rutile destabilization. This destabilization occurred presumably only during the second stage of the rodingitization (see above) and led to the precipitation of titanite and Ti-rich garnet and vesuvianite.

5.4 Control on vesuvianite stability

Vesuvianite is particularly abundant in rodingites from Bôrček and represents one of the most interesting feature of these samples. Several factors may have enhanced vesuvianite formation during rodingite metasomatism. Murzin et al. (2013) have proposed that Al-rich protoliths tend to produce vesuvianite-rich rodingites, and vice versa. However, this is not consistent with the fact that even Ti-rich (and thus Al-low) rodingite samples from Bôrček (e.g. FBR-57) are also dominated by vesuvianite (Fig. 2b). Some other authors (Li et al., 2008; Panseri et al., 2008) have suggested that vesuvianite forms under high P-T conditions and consequently represents an exclusively metamorphic mineral that forms in subduction environments. Thermodynamic modelling investigating vesuvianite indicates, however, that its stability range is too wide to reliably constrain the P-T conditions of its formation (e.g. Li et al., 2007). Moreover, vesuvianite was also exceptionally reported from present-day ocean floor (Honnorez and Kirst, 1975) where high P-T conditions cannot be considered as the key agent to induce the formation of vesuvianite. CO_2 concentration in the hydrothermal fluid is another parameter to be considered. Thermodynamic calculations indicates that CO_2 have to be very low ($X_{CO2} < 10^{-4}$) to allow the formation of vesuvianite (Duan et al., 2021; Li et al., 2008). However, Salvioli-Mariani et al. (2020) show that low CO_2 concentration is not required to stabilize vesuvianite and CO_2 concentration is thus not a limiting factor. In the rodingites from Bôrček, we suggest that the most abundant vesuvianite I formed under fluid saturated conditions with low CO_2 concentration, low SiO_2 and high CaO activities, while vesuvianite II formed by recrystallization more or less in situ despite higher CO_2 concentration in the late hydrothermal fluid.

At last, several studies focusing on the evolution of rodingite paragenesis (Li et al., 2017; Salvioli-Mariani et al., 2020; Schandl et al., 1989) propose that high CaO and low SiO_2 activities are needed to stabilize vesuvianite, which implies that intense (long-lasting) Ca-metasomatism is indispensable for the vesuvianite crystallization. The compilation of data presented in Figure 15 document such an extensive metasomatism for vesuvianite-bearing rodingites. The intensity of the metasomatic process which lead to a major change in whole-rock chemistry and specifically low SiO_2 and high CaO activity is thus our favored explanation for the high richness in vesuvianite of the rodingites from the Bôrček locality.

6 Conclusions

- Rodingites from Bôrček (Western Carpathians) consist of vesuvianite, diopside, and hydrated garnet with minor titanite, chlorite, epidote, calcite, and Fe-Ti oxides.
- Despite the lack of primary minerals and textures, the high Al_2O_3 content and vesuvianite REE patterns suggest a plagioclase-rich protolith. Furthermore, the Fe-Ti rich aggregates in some samples (whole rock TiO_2 up to 9.2 wt.%) indicate that the protolith was presumable a Fe-Ti rich gabbroic rock that commonly occurs in the oceanic lithosphere. Ti-poor samples with lower trace element concentrations and higher Mg number would originate from a gabbroic protolith with a more common magnesian composition.
- The primary minerals were affected by an intense rodingitization, resulting in complete replacement with vesuvianite, diopside, and minor garnet. Second generations of vesuvianite and garnet are particularly rich in Ti and indicate a second rodingitization stage during which Ti was presumably supplied by rutile and ilmenite alteration. Titanite formed as reaction rims around these Fe-Ti accumulations. Later vesuvianite occurs in veins and veinlets either as a monomineral filling or with minor chlorite. The last hydrothermal event is characterized by the formation of an epidote-chlorite-calcite assemblage, which probably documents the alpine regional metamorphism under greenschist facies conditions.
- Vesuvianite represents the main carrier of trace elements in the investigated rodingites from Bôrček. Whole rock analyses indicate an intense metasomatic process characterized by Ca-enrichment and Si-K-Na leaching which is in good agreement with the traditional notion of rodingitization. However, more detailed studies are required to constrain P-T conditions, and mainly fluid composition, inducing the formation of these particular mineral assemblages.

Aksenov, S.M., Chukanov, N.V., Rusakov, V.S., Panikorovskii, T.L., Rastsvetaeva, R.K., Gainov, R.R., Vagizov, F.G., Lyssenko, K.A., Belakovskiy, D.I., 2016. Towards a revisitation of vesuvianite-group nomenclature: the crystal structure of Ti-rich vesuvianite from Alchuri, Shigar Valley. Acta Crystallogr. Sect. B Struct. Sci. Cryst. Eng. Mater. 72, 744–752. https://doi.org/10.1107/S2052520616010246

Armbruster, T., Bonazzi, P., Akasaka, M., Bermanec, V., Chopin, C., Gieré, R., Heuss-Assbichler, S., Liebscher, A., Menchetti, S., Pan, Y., Pasero, M., 2006. Recommended nomenclature of epidote-group minerals. Eur. J. Mineral. 18, 551–567. https://doi.org/10.1127/0935-1221/2006/0018-0551

Attoh, K., Evans, M.J., Bickford, M.E., 2006. Geochemistry of an ultramafic-rodingite rock association in the Paleoproterozoic Dixcove greenstone belt, southwestern Ghana. J. Afr. Earth Sci. 45, 333–346. https://doi.org/10.1016/j.jafrearsci.2006.03.010

Austrheim, H., Prestvik, T., 2008. Rodingitization and hydration of the oceanic lithosphere as developed in the Leka ophiolite, north–central Norway. Lithos 104, 177–198. https://doi.org/10.1016/j.lithos.2007.12.006

Bajaník, Š., Planderová, E., 1985. Stratigrafická pozícia spodnej časti ochtinského súvrstvia gemerika medzi Magnezitovcami a Magurou. Geol. Práce Správy 82, 67–76.

Barriga, F., Fyfe, W.S., 1983. Development of rodingite in basaltic rocks in serpentinites, East Liguria, Italy. Contrib. Mineral. Petrol. 84, 146–151. https://doi.org/10.1007/BF00371281

Bidyananda, M., Sharma, K.A., Shukla, A.D., Kapsiotis, A., Belousova, E., 2021. Geochemical and geochronological study of rodingites from the northeast India ophiolites: Petrogenetic significance and timing of rodingitization. Geol. J. n/a, 1–14. https://doi.org/10.1002/gj.4301

Bilgrami, S.A., Howie, R.A., 1960. The mineralogy and petrology of a rodingite dike, Hidubagh. Pakistan. Am. Mineral. 45, 791–801.

Bocchio, R., Benciolini, L., Martin, S., Tartarotti, P., 2000. Geochemistry of eclogitised Fe-Ti-gabbros from various lithological settings (Aosta Valley ophiolites, Italian western Alps). Protolith composition and eclogitic paragenesis. Period. Mineral. 69, 217–237.

Bucher, K., Grapes, R., 2009. The Eclogite-facies Allalin Gabbro of the Zermatt-Saas Ophiolite, Western Alps: a Record of Subduction Zone Hydration. J. Petrol. 50, 1405–1442. https://doi.org/10.1093/petrology/egp035

Bucher, K., Stober, I., 2021. Metamorphic gabbro and basalt in ophiolitic and continental nappes of the Zermatt region (Western Alps). Swiss J. Geosci. 114, 12. https://doi.org/10.1186/s00015-021-00390-w

Butek, J., Spišiak, J., Milovská, S., 2021. Garnet-Vesuvianite Equilibrium in Rodingites from Dobšiná (Western Carpathians). Minerals 17.

Coleman, R.G., 1967. Low-temperature reaction zones and alpine ultramafic rocks of California, Oregon, and Washington. Geol. Surv. Bull. https://doi.org/10.3133/b1247

Dai, J.G., Wang, C.S., Liu, S.A., Qian, X.Y., Zhu, D.C., Ke, S., 2016. Deep carbon cycle recorded by calcium-silicate rocks (rodingites) in a subduction-related ophiolite: Deep Carbon Cycle Recorded by Rodingite. Geophys. Res. Lett. 43, 11,635-11,643. https://doi.org/10.1002/2016GL070474

Duan, W.-Y., Li, X.-P., Schertl, H.-P., Willner, A.P., Wang, S.-J., Chen, S., Sun, G.-M., 2022. Rodingitization records from ocean-floor to high pressure metamorphism in the Xigaze ophiolite, southern Tibet. Gondwana Res., Metamorphism and Magmatism of the Tibetan Plateau and Tethys evolution 104, 126–153. https://doi.org/10.1016/j.gr.2021.05.013

Duan, W.-Y., Li, X.-P., Wang, Z.-L., Chen, S., Sun, G.-M., Zhao, L.-Q., 2021. Thermodynamic modeling and elemental migration for the early stage of rodingitization: An example from the Xialu massif of the Xigaze ophiolite, southern Tibet. Geosci. Front. 12, 101–125. https://doi.org/10.1016/j.gsf.2020.12.006

Dubińska, E., Bylina, P., Kozłowski, A., Dörr, W., Nejbert, K., Schastok, J., Kulicki, C., 2004. U–Pb dating of serpentinization: hydrothermal zircon from a metasomatic rodingite shell (Sudetic ophiolite, SW Poland). Chem. Geol. 203, 183–203. https://doi.org/10.1016/j.chemgeo.2003.10.005

El-Shazly, A.K., Al-Belushi, M., 2004. Petrology and Chemistry of Metasomatic Blocks from Bawshir, Northeastern Oman. Int. Geol. Rev. 46, 904–938. https://doi.org/10.2747/0020-6814.46.10.904

Esteban, J.J., Cuevas, J., Tubia, J.M., Yusta, I., 2003. Xonotlite in rodingite assemblages from the Ronda peridotites, Betic Cordilleras, southern Spain. Can. Mineral. 41, 161–170. https://doi.org/10.2113/gscanmin.41.1.161

Evans, B.W., Trommsdorff, V., Goles, G.G., 1981. Geochemistry of high-grade eclogites and metarodingites from the Central Alps. Contrib. Mineral. Petrol. 76, 301–311. https://doi.org/10.1007/BF00375457

Ferrando, S., Frezzotti, M.L., Orione, P., Conte, R.C., Compagnoni, R., 2010. Late-Alpine rodingitization in the Bellecombe meta-ophiolites (Aosta Valley, Italian Western Alps): evidence from mineral assemblages and serpentinization-derived H_2 -bearing brine. Int. Geol. Rev. 52, 1220–1243. https://doi.org/10.1080/00206810903557761

Froitzheim, N., Plasienka, D., Schuster, R., 2008. Alpine tectonics of the Alps and Western Carpathians, in: McCann, T. (Ed.), The Geology of Central Europe Volume 2: Mesozoic and Cenozoic. The Geological Society of London, pp. 1141–1232. https://doi.org/10.1144/CEV2P.6

Fukuyama, M., Ogasawara, M., Dunkley, D.J., Wang, K.-L., Lee, D.-C., Hokada, T., Maki, K., Hirata, T., Kon, Y., 2014. The formation of rodingite in the Nagasaki metamorphic rocks at Nomo Peninsula, Kyushu, Japan - Zircon U-Pb and Hf isotopes and trace element evidence: Formation of rodingite. Isl. Arc 23, 281–298. https://doi.org/10.1111/iar.12086

Geologická mapa Slovenska M 1:50 000 [online]. Bratislava: Štátny geologický ústav Dionýza Štúra. [WWW Document], 2013. . http://apl.geology.sk/gm50js.

Govindaraju, K., Roelandts, I., 1989. 1988 Compilation report on trace elements in six ANRT rock reference samples: diorite DR-N, serpentine UB-N, bauxite BX-N, granite GS-N and potash feldspar FK-N. Geostand. Geoanalytical Res. 13, 5–67. https://doi.org/10.1111/j.1751-908X.1989.tb00465.x

Griffin, W.L., Powell, W.J., Pearson, N.J., O'Reilly, S.Y., 2008. GLITTER : Data reduction software for laser ablation ICP-MS, in: Laser Ablation ICP-MS in the Earth Sciences : Current Practices and Outstanding Issues, Short Course (Book 40). Mineralogical Association of Canada, Vancouver, pp. 308–311.

Groat, L.A., Hawthorne, F.C., Ercit, T.S., 1992. The chemistry of vesuvianite. Can. Mineral. 30, 19–48.

Haws, A.A., Starr, P.G., Dragovic, B., Scambelluri, M., Belmonte, D., Caddick, M.J., Broadwell, K.S., Ague, J.J., Baxter, E.F., 2021. Meta-rodingite dikes as recorders of subduction zone metamorphism and serpentinite dehydration: Voltri Ophiolite, Italy. Chem. Geol. 565, 120077. https://doi.org/10.1016/j.chemgeo.2021.120077

Honnorez, J., Kirst, P., 1975. Petrology of rodingites from the equatorial Mid-Atlantic fracture zones and their geotectonic significance. Contrib. Mineral. Petrol. 49, 233–257. https://doi.org/10.1007/BF00376590

Hovorka, D., Dubíková, K., Gerthofferová, H., Šamajová, E., Turan, J., 1983. Serpentine-group minerals of the West Carpathian ultramafics. II -Bodies in Pre-Mesozoic metamorphosed complexes.pdf. Miner. Slovaca 15, 23–47.

Hovorka, D., Ivan, P., Jaroš, J., Kratochvíl, M., Reichwalder, P., Rojkovič, I., Spišiak, J., Turanová, L., 1985. Ultramafic Rocks of the Western Carpathians / Czechoslovakia. GÚDŠ, Bratislava.

Hu, C.-N., Santosh, M., 2018. Devonian rodingite from the northern margin of the North China Craton: mantle wedge metasomatism during ocean-continent convergence. Int. Geol. Rev. 60, 1073–1097. https://doi.org/10.1080/00206814.2017.1365631

Karkalis, C., Magganas, A., Koutsovitis, P., Pomonis, P., Ntaflos, T., 2022. Multiple Rodingitization Stages in Alkaline, Tholeiitic, and Calc-Alkaline Basaltic Dikes Intruding Exhumed Serpentinized Tethyan Mantle from Evia Island, Greece. Lithosphere 2022, 9507697. https://doi.org/10.2113/2022/9507697

Kobayashi, S., Kaneda, H., 2010. Rodingite with Ti- and Cr-rich vesuvianite from the Sartuohai chromium deposit, Xinjiang, China. J. Mineral. Petrol. Sci. 105, 112–122. https://doi.org/10.2465/jmps.081224

Koutsovitis, P., 2017. High-pressure subduction-related serpentinites and metarodingites from East Thessaly (Greece): Implications for their metamorphic, geochemical and geodynamic evolution in the Hellenic–Dinaric ophiolite context. Lithos, European Lithospheric Mantle; geochemical, petrological and geophysical processes 276, 122–145. https://doi.org/10.1016/j.lithos.2016.11.008

Koutsovitis, P., Magganas, A., Pomonis, P., Ntaflos, T., 2013. Subduction-related rodingites from East Othris, Greece: Mineral reactions and physicochemical conditions of formation. Lithos 172–173, 139–157. https://doi.org/10.1016/j.lithos.2013.04.009

Kozur, H., 1991. The evolution of the Meliata-Hallstatt ocean and its significance for the early evolution of the Eastern Alps and Western Carpathians. Palaeogeogr. Palaeoclimatol. Palaeoecol. 87, 109–135. https://doi.org/10.1016/0031-0182(91)90132-B

Laborda-López, C., López-Sánchez-Vizcaíno, V., Marchesi, C., Gómez-Pugnaire, M.T., Garrido, C.J., Jabaloy-Sánchez, A., Padrón-Navarta, J.A., Hidas, K., 2018. High- *P* metamorphism of rodingites during serpentinite dehydration (Cerro del Almirez, Southern Spain): Implications for the redox state in subduction zones. J. Metamorph. Geol. 36, 1141–1173. https://doi.org/10.1111/jmg.12440

Laborda-López, C., Marchesi, C., López Sánchez-Vizcaíno, V., Gómez-Pugnaire, M.T., Dale, C.W., Jabaloy-Sánchez, A., Padrón-Navarta, J.A., Román-Alpiste, M.J., Garrido, C.J., 2020. Geochemical evolution of rodingites during subduction: insights from Cerro del Almirez (southern Spain). Lithos 370–371, 105639. https://doi.org/10.1016/j.lithos.2020.105639

Lesnov, F.P., 2010. Rare Earth Elements in Ultramafic and Mafic Rocks and their Minerals: Main types of rocks. Rock-forming minerals. CRC Press.

Li, X.-H., Putiš, M., Yang, Y.-H., Koppa, M., Dyda, M., 2014. Accretionary wedge harzburgite serpentinization and rodingitization constrained by perovskite U/Pb SIMS age, trace elements and Sm/Nd isotopes: Case study from the Western Carpathians, Slovakia. Lithos 205, 1–14. https://doi.org/10.1016/j.lithos.2014.06.001

Li, X.-P., Duan, W.-Y., Zhao, L.-Q., Schertl, H.-P., Kong, F.-M., Shi, T.-Q., Zhang, X., 2017. Rodingites from the Xigaze ophiolite, southern Tibet – new insights into the processes of rodingitization. Eur. J. Mineral. 29, 821–837. https://doi.org/10.1127/ejm/2017/0029-2633

Li, X.-P., Rahn, M., Bucher, K., 2008. Eclogite facies metarodingites – phase relations in the system SiO_2-Al_2O_3-Fe_2O_3-FeO-MgO-CaO-CO_2-H_2O: an example from the Zermatt-Saas ophiolite. J. Metamorph. Geol. 26, 347–364. https://doi.org/10.1111/j.1525-1314.2008.00761.x

Li, X.-P., Rahn, M., Bucher, K., 2004. Metamorphic Processes in Rodingites of the Zermatt-Saas Ophiolites. Int. Geol. Rev. 46, 28–51. https://doi.org/10.2747/0020-6814.46.1.28

Li, X.-P., Zhang, L., Wei, C., Ai, Y., Chen, J., 2007. Petrology of rodingite derived from eclogite in western Tianshan, China. J. Metamorph. Geol. 25, 363–382. https://doi.org/10.1111/j.1525-1314.2007.00700.x

Liou, J.G., Zhang, R., Ernst, W.G., 1998. Mineral parageneses in the Piampaludo eclogitic body, Gruppo di Voltri, Western Ligurian Alps. https://doi.org/10.5169/SEALS-59291

Lorand, J.-P., Gregoire, M., 2010. Petrogenesis of Fe–Ti oxides in amphibole-rich veins from the Lherz orogenic peridotite (Northeastern Pyrénées, France). Contrib. Mineral. Petrol. 160, 99–113. https://doi.org/10.1007/s00410-009-0468-4

MacLeod, C.J., Dick, H.J., Blum, P., 2017. Site U1473, in: Proceedings of the International Ocean Discovery Program, Proceedings of the International Ocean Discovery Program. International Ocean Discovery Program. https://doi.org/10.14379/iodp.proc.360.2017

McCarthy, A., Müntener, O., 2019. Evidence for ancient fractional melting, cryptic refertilization and rapid exhumation of Tethyan mantle (Civrari Ophiolite, NW Italy). Contrib. Mineral. Petrol. 174, 69. https://doi.org/10.1007/s00410-019-1603-5

McDonough, W.F., Sun, S. -s., 1995. The composition of the Earth. Chem. Geol. 120, 223–253.

Miller, C., Zanetti, A., Thöni, M., Konzett, J., 2007. Eclogitisation of gabbroic rocks: Redistribution of trace elements and Zr in rutile thermometry in an Eo-Alpine subduction zone (Eastern Alps). Chem. Geol. 239, 96–123. https://doi.org/10.1016/j.chemgeo.2007.01.001

Mohammad, Y.O., Maekawa, H., 2008. Origin of titanite in metarodingite from the Zagros Thrust Zone, Iraq. Am. Mineral. 93, 1133–1141. https://doi.org/10.2138/am.2008.2580

Montanini, A., Travaglioli, M., Serri, G., Dostal, J., Ricci, C.A., 2006. Petrology Of Gabbroic To Plagiogranitic Rocks From Southern Tuscany (Italy): Evidence For Magmatic Differentation In An Ophiolitic Sequence. Ofioliti 31, 55–69.

Morimoto, N., 1988. Nomenclature of pyroxenes. Bull. Minéralogie 111, 535–550. https://doi.org/10.3406/bulmi.1988.8099

Mubarak, H.S., Azer, M.K., Surour, A.A., Moussa, H.E., Asimow, P.D., Kabesh, M.M.L., 2020. Mineralogical and geochemical study of rodingites and associated serpentinized peridotite, Eastern Desert of Egypt, Arabian-Nubian Shield. Lithos 374–375, 105720. https://doi.org/10.1016/j.lithos.2020.105720

Murzin, V.V., Varlamov, D.A., Ronkin, Yu.L., Shanina, S.N., 2013. Origin of Au-bearing rodingite in the Karabash massif of alpine-type ultramafic rocks in the southern Urals. Geol. Ore Depos. 55, 278–297. https://doi.org/10.1134/S1075701513040053

Nishiyama, T., Yoshida-Shiosaki, C., Mori, Y., Shigeno, M., 2017. Interplay of irreversible reactions and deformation: a case of hydrofracturing in the rodingite-serpentinite system. Prog. Earth Planet. Sci. 4, UNSP 1. https://doi.org/10.1186/s40645-016-0115-4

Normand, C., Williams-Jones, A.E., 2007. Physicochemical conditions and timing of rodingite formation: evidence from rodingite-hosted fluid inclusions in the JM Asbestos mine, Asbestos, Québec. Geochem. Trans. 8, 11. https://doi.org/10.1186/1467-4866-8-11

Panseri, M., Fontana, E., Tartarotti, P., 2008. Evolution of rodingitic dykes: metasomatism and metamorphism in the Mount Avic serpentinites (alpine ophiolites, southern Aosta valley). Ofioliti 33, 165–185.

Piber, A., Tropper, P., 2010. Ba-Ti-bearing metarodingites from the Austroalpine units (Innsbruck Quartzphyllite, Wildschönau Schists) north of the Tauern Window (Tyrol, Eastern Alps, Austria). Neues Jahrb. Für Mineral. - Abh. 187, 189–205. https://doi.org/10.1127/0077-7757/2010/0170

Plašienka, D., 2018. Continuity and Episodicity in the Early Alpine Tectonic Evolution of the Western Carpathians: How Large-Scale Processes Are Expressed by the Orogenic Architecture and Rock Record Data. Tectonics 37, 2029–2079. https://doi.org/10.1029/2017TC004779

Plašienka, D., Méres, Š., Ivan, P., Sýkora, M., Soták, J., Lačný, A., Aubrecht, R., Bellová, S., Potočný, T., 2019. Meliatic blueschists and their detritus in Cretaceous sediments: new data constraining tectonic evolution of the West Carpathians. Swiss J. Geosci. 112, 55–81. https://doi.org/10.1007/s00015-018-0330-7

Putiš, M., Yang, Y.-H., Vaculovič, T., Koppa, M., Li, X.-H., Uher, P., 2016. Perovskite, reaction product of a harzburgite with Jurassic– Cretaceous accretionary wedge fluids (Western Carpathians, Slovakia): evidence from the whole-rock and mineral trace element data. Geol. Carpathica 67, 135–148. https://doi.org/10.1515/geoca-2016-0009

Python, M., Ceuleneer, G., Ishida, Y., Barrat, J.-A., Arai, S., 2007. Oman diopsidites: a new lithology diagnostic of very high temperature hydrothermal circulation in mantle peridotite below oceanic spreading centres. Earth Planet. Sci. Lett. 255, 289–305. https://doi.org/10.1016/j.epsl.2006.12.030

Rogkala, A., Petrounias, P., Koutsovitis, P., Giannakopoulou, P.P., Pomonis, P., Lampropoulou, P., Hatzipanagiotou, K., 2022. Rodingites from the Veria-Naousa ophiolite (Greece): Mineralogical evolution, metasomatism and petrogenetic processes. Geochemistry 125860. https://doi.org/10.1016/j.chemer.2021.125860

Roth, C.B., 1969. Deferration Effect on Structural Ferrous-Ferric Iron Ratio and CEC of Vermiculites and Soils. Clays Clay Miner. 17, 253–264. https://doi.org/10.1346/CCMN.1969.0170502

Salvioli-Mariani, E., Boschetti, T., Toscani, L., Montanini, A., Petriglieri, J.R., Bersani, D., 2020. Multi-stage rodingitization of ophiolitic bodies from Northern Apennines (Italy): Constraints from petrography, geochemistry and thermodynamic modelling. Geosci. Front. 11, 2103–2125. https://doi.org/10.1016/j.gsf.2020.04.017

Sassi, F.P., Vozárová, A., 1987. The pressure cahracter of the Hercynian metamorphism in the Gemercium (West Carpathians, Czechoslovakia). Rendiconti Della Soc. Ital. Mineral. E Petrol. 42, 73–81.

Schandl, E.S., O'Hanley, D.S., Wicks, F.J., 1989. Rodingites in serpentinized ultramafic rocks of the Abitibi Greenstone belt, Ontario. Can. Mineral. 27, 579–591.

Schulte, B., Sindern, S., 2002. K-rich fluid metasomatism at high-pressure metamorphic conditions: Lawsonite decomposition in rodingitized ultramafite of the Maksyutovo complex, Southern Urals (Russia). J. Metamorph. Geol. 20, 529–541. https://doi.org/10.1046/j.1525-1314.2002.00387.x

Schwartz, S., Lardeaux, J.-M., Guillot, S., Tricart, P., 2000. Diversité du métamorphisme éclogitique dans le massif ophiolitique du Monviso (Alpes occidentales, Italie). Geodin. Acta 13, 169–188. https://doi.org/10.1080/09853111.2000.11105371

Spišiak, J., Mikuš, T., Butek, J., 2018. Topás-andaluzit-korundová varieta rodingitov(?) z Brezničky (Ochtinská skupina, Západné Karpaty, Slovensko). Bull. Mineral. Petrol. 26, 57–63.

Starr, P.G., Broadwell, K.S., Dragovic, B., Scambelluri, M., Haws, A.A., Caddick, M.J., Smye, A.J., Baxter, E.F., 2020. The subduction and exhumation history of the Voltri Ophiolite, Italy: Evaluating exhumation mechanisms for high-pressure metamorphic massifs. Lithos 376–377, 105767. https://doi.org/10.1016/j.lithos.2020.105767

Tang, Y., Zhai, Q.-G., Hu, P.-Y., Wang, J., Xiao, X.-C., Wang, H.-T., Tang, S.-H., Lei, M., 2018. Rodingite from the Beila ophiolite in the Bangong–Nujiang suture zone, northern Tibet: New insights into the formation ofophiolite-related rodingite. Lithos 316–317, 33–47. https://doi.org/10.1016/j.lithos.2018.07.006

Tsikouras, B., Karipi, S., Hatzipanagiotou, K., 2013. Evolution of rodingites along stratigraphic depth in the Iti and Kallidromon ophiolites (Central Greece). Lithos 175–176, 16–29. https://doi.org/10.1016/j.lithos.2013.04.021

Wang, S., Li, X.-P., Duan, W., Kong, F., Wang, Z., 2019. Record of Early-Stage Rodingitization from the Purang Ophiolite Complex, Western Tibet. J. Earth Sci. 30, 1108–1124. https://doi.org/10.1007/s12583-019-1244-7

Whitney, D.L., Evans, B.W., 2010. Abbreviations for names of rock-forming minerals. Am. Mineral. 95, 185–187. https://doi.org/10.2138/am.2010.3371

Yavuz, F., Kumral, M., Karakaya, N., Karakaya, M.Ç., Yıldırım, D.K., 2015. A Windows program for chlorite calculation and classification. Comput. Geosci. 81, 101–113. https://doi.org/10.1016/j.cageo.2015.04.011

Zanoni, D., Rebay, G., Spalla, M.I., 2016. Ocean floor and subduction record in the Zermatt-Saas rodingites, Valtournanche, Western Alps. J. Metamorph. Geol. 34, 941–961. https://doi.org/10.1111/jmg.12215

Zlocha, J., Rusinová, J., Valko, P., 1980. Záverečná správa a výpočet zásob, Kalinovo - VP, chryzotilový azbest. Slovenský geologický úrad Bratislava, Geologický prieskum, n. p., Spišská Nová Ves, Geologická oblasť Rožňava.